THE EFFECT OF WIND AND MOMENTUM ADVECTION IN THE JAMES RIVER ESTUARY FROM FIELD OBSERVATIONS

By

JIGE GUO

A thesis submitted to the

Graduate School-New Brunswick

Rutgers, The State University of New Jersey

in partial fulfillment of the requirements

for the degree of

Master of Science

Graduate Program in Oceanography

written under the direction of

Robert Chant

and approved by

_____

_____

_____

New Brunswick, New Jersey

[January 2012]

ABSTRACT OF THE THESIS

The Effect of Wind and Momentum Advection in the James River Estuary from Field Observations

by JIGE GUO

Thesis Director:

Robert Chant

From moorings deployed to the lower part of the James River (the southernmost tributary to the Chesapeake Bay), time series of velocity, salinity and pressure are collected for a length of 40 days. The time period covers one full spring and neap tide and both high wind and low wind scenarios. The velocity field, notably the lateral velocity and the calculated vertical velocity, as well as the salinity field are examined both spatially and temporally along a cross channel transect. Major findings include clear spring-neap variation in the lateral flow and little spring-neap variation in the longitudinal flow, persistent southward residual flow in the cross channel direction, tidal asymmetry in the vertical velocity, and tidal/subtidal variation in the salinity field.

The wind effect is seen from augmented exchange flow and stratification after strong down estuary wind and weakened exchange flow and stratification after strong up estuary wind. It also impacts the lateral flow through Ekman dynamics as the down estuary wind introduces max southward flow and up estuary wind brings max northward flow in the cross channel direction.

The role of advective acceleration in this estuary is examined through the momentum budget which includes three advective acceleration terms and two pressure gradient terms calculated from the data and the vertical stress divergence term inferred from the momentum balance. The outstanding advection comes from the second half of the ebb tide with different signs over different sides of the main channel. On both subtidal and tidal scales, it accelerates the along channel flow seaward over the southern shoal and landward over the northern channel and therefore superimposes additional residual flow structure to

the along channel flow. The results, especially the advective acceleration being in the first order momentum balance in the upper layer, demonstrate that the along channel momentum balance is more complex than previously thought.

ACKNOWLEDGEMENT

I would like to thank my advisor Robert Chant for his guidance and assistance during the thesis work as well as through my graduate study in the program. Thank fellow graduate students Maria Aristizabal and Joseph Jurisa for their help in discussing various problems and offering valuable suggestions throughout the thesis writing. Thank Eli Hunter for his assistance with data preparation and problem solving. Thank the program director John Wilkin for the exhortation in the beginning of the writing and all my committee members (Robert Chant, John Wilkin and Josh Kohut) for their invaluable insights on the thesis.

List of Contents

Table of Contents

ABSTRACT OF THE THESIS ii

ACKNOWLEDGEMENT iv

List of Contents v

List of Illustrations vii

Introduction 1

Data Description 3

Estuarine conditions 4

Method 6

Estimating the pressure gradient 6

Estimating the advective acceleration terms 7

Estimating vertical stresses 9

Results 10

Mean conditions 10

Mean subtidal flow 10

Mean tidal flow 11

Mean salinity field 12

Time series and the influence of wind 13

Time series of the subtidal flow 13

Time series of the subtidal density 15

Influence of wind....16
Tidal period variation during low wind, spring tide....18
Tidal period variation of velocities....19
The momentum budget....20
Along channel momentum budget....21
Cross channel momentum budget....27
Discussion....28
Advection seen in the along channel momentum budget....28
Advection seen in the salt field....29
Summary....30
Figures....33
References....53

List of Illustrations

Figure 1: The James River estuary and field instrument locations. (a): The James River estuary in the context of Chesapeake Bay. The magenta rectangle marks the area of the lower estuary. (b): Map of the experiment site. The red dots show the locations of the moorings and the green rectangle marks the area of the mooring array. The blue dot indicates the location of NOAA tidal station at Sewells Point. (c): The mooring array in 2 lines with red clustered arrows showing surface velocity. The light blue shaded area indicates the shallow shoals. The James River Bridge is shown in the lower right of the chart. (d-e): Locations of 3 types of instruments deployed along the 2 lines. X-axis is the distance from the E mooring with unit 'm' and y-axis is depth below the surface also with unit 'm'. A line (L1A-L2A) is referred to the northern channel, B line (L1B-L2B) is referred to the main channel and the C, D, and E lines are referred to the southern shoal in this paper. 33

Figure 2: Duration of field data from ADCP and CTD sensors. Upper panel shows the duration of ADCP data with instrument locations labeled on the left; lower panel shows the duration of CTD data with sensor locations labeled on the left and sensor depths (below surface) indicated on the right. 34

Figure 3: Time series showing estuarine conditions during the experiment period. The top panel is the river discharge and the red dot marks the time when the discharge started to increase. The second panel shows water level at Sewells Point with the green dots indicating spring tide and the magenta dots indicating neap tide. The black line is the tidally averaged water level. The lower two panels show the time series of winds and the red dots denote times of extreme winds. Positive direction is downstream for along channel wind and northward for cross channel wind. 35

Figure 4: The average conditions of subtidal velocities over transect 1 (looking into the estuary). The color filled contours describe along channel velocities and the vectors scale with the across channel velocities. The thick white lines indicate zero along channel velocity. The along channel, across channel and vertical velocities are in different units as shown in the figure. 36

Figure 5: The average conditions of velocities over transect 1 (looking into the estuary) at the maximum flood and ebb tide. The color filled contours describe along channel velocities and the vectors scale with the across channel velocities. The along channel, across channel and vertical velocities are in different units as shown in the figure. Note that the color bars have different ranges between maximum flood and ebb for the along channel velocity. 37

Figure 6: Interpolated salinity plot for transect 1. Every panel shows the temporal average of salinity during the tidal condition indicated in its individual title. Contours are in the unit of psu and color bars have the same range from 12 psu to 21 psu. Note that panel (a) and (b) are contoured every 0.5 psu while panel (c) and (d) are contoured every 1 psu. 38

Figure 7: Time series of along channel and across channel subtidal flow. In the upper panel, along channel flow (exchange flow) was integrated over transect 1 with subtidal velocities from ADCPs L1E, L1D, L1C, L1B and L1A. Positive is out flow from the estuary in the upper layer and negative is in flow to the estuary in the lower layer. The lateral circulation is shown in the lower panel with northward flow and southward flow both averaged over transect 1. The red dots indicate time of extreme flows and the dashed lines show the flow magnitude in all directions during these times. Time stamps when the extreme flow occurred are also provided. 39

Figure 8: Time series of subtidal densities from all the CTD sensors along the two lines (see Figure 1 for instruments layout). Legend for line 1 is on top of the figure; legend for line 2 is in the bottom panel. Shaded areas are during neap tides. The start time of the longer arrows and time of the shorter arrows are shown in the lower panel. All solid lines are time series of surface densities and dashed lines are densities from the bottom and mid-depth. 40

Figure 9: Velocity and salinity snap shots on subtidal scale over transect 1 (looking into the estuary). (a-d): Snap shots of velocity at times indicated in its individual titles. The color filled contours describe along channel velocities and the vectors scale with cross channel velocities. The thick white lines mark zero along channel velocity. The along channel, cross channel and vertical velocities are in different units as

shown in the figure. (e-f): Snap shots of interpolated salinity at times indicated in its individual titles. Contours are in the unit of psu and color bars have the same range from 13 psu to 23 psu. Note that panel (e) is contoured every 1 psu while panel (f) is contoured every 0.5 psu. 41

Figure 10: Time series of sea level, velocity and density during the low wind, spring period. Red dots mark max flood; green dots mark max ebb. Magenta dots represent slack after flood and cyan dots represent slack after ebb. (a): Time series of water level at Sewells Point (location shown in Figure 1 (b)). (b): Time series of depth averaged along channel velocity at L1A. Black solid line is low pass filtered velocity. (c): Time series of density at mid-depth of L1D. 42

Figure 11: Velocity profiles averaged over the low wind, spring tide period following the tidal phases in Figure 10. The location of the moorings is indicated by their IDs on the left and the phases in the tidal cycle are shown on the top. Blue line is the along channel velocity and red line is the cross channel velocity. Their values are both shown on the bottom of each individual panel with bounds [-0.7 0.7] m/s. The green line is vertical velocity calculated from both du/dx and dv/dy and the yellow line is vertical velocity calculated using only dv/dy. Their values are indicated on the top of each panel with the green ticks. The unit is also m/s. The y-axis is depth below water surface and has the unit of m.....43

Figure 12: A schematic view of the velocity field at max flood and ebb. Blue circles represent along channel velocity, red arrows represent cross channel velocity and green arrows represent vertical velocity. The sizes of the shapes are drawn to show the relative speed in each direction, but no comparison of magnitude should be made among different directions.....44

Figure 13: The relation between along channel bottom stress integrated from the momentum equation (τxb) and bottom stress calculated from quadratic drag law ($\rho ubub$) indicates the estimated bottom drag CD. The unit for both axes is $kgm3 \times m2s2$. The green line is the best linear fit and its slope is the estimated CD for the location shown. The correlation coefficient is also shown. 45

Figure 14: Stress profiles averaged at four tidal phases over the low wind, spring tide piece. 46

Figure 15: Subtidal forces in the along channel momentum equation (Eq.3) averaged during the low wind, spring tide piece for the 3 locations. Solid lines represent different individual terms in the momentum equation; Thick slash lines describe the sum of similar terms. Unit for x-axis is $kgm3 \times ms2$ and unit for y-axis is m (depth below water surface). 47

Figure 16: Forces in the along channel momentum equation averaged over the four tidal phases at the three moorings. Colors represent difference terms in Eq.3. Unit for x-axis is $kgm3 \times ms2$ and unit for y-axis is m (depth below water surface). 48

Figure 17: Forces in the along channel momentum equation averaged over the four tidal phases at the three moorings. Solid lines represent different individual terms in the momentum equation; thick slash lines describe the sum of similar terms. Unit for x-axis is $kgm3 \times ms2$ and unit for y-axis is m (depth below water surface).....49

Figure 18: Subtidal forces in the cross channel momentum equation (Eq.3) averaged during the low wind, spring tide piece for the 3 locations. Colors represent different individual terms in the momentum equation Unit for x-axis is $kgm3 \times ms2$ and unit for y-axis is m (depth below water surface).....50

Figure 19: Forces in the cross channel momentum equation averaged over the four tidal phases at the three moorings. Colors represent difference terms in Eq.3. Unit for x-axis is $kgm3 \times ms2$ and unit for y-axis is m (depth below water surface). 51

Figure 20: Scopes of salinity fluctuation averaged within tidal cycles over the whole record. The unit is psu. The numbers and colors indicate the magnitude of the difference between maximum salinity and minimum salinity during the tidal cycle. 52

Introduction

As the southernmost tributary to the Chesapeake Bay, the James River estuary is categorized as a coastal plain estuary (NOAA 2008) and has been a place of research interest for over a half century. In one of the pioneering studies (Pritchard 1956), Pritchard managed to quantify some forces in the momentum equation with limited data. He concluded that in the longitudinal (along channel) direction, the pressure gradient force is primarily balanced by the frictional force. In the lateral (cross channel) direction, the Coriolis force is balanced primarily by the lateral pressure gradient force and secondarily by the frictional force. Using a linearized shear stress term with constant eddy viscosity, A_v, Hansen & Rattray (1965) were able to solve the first order along channel momentum equation (pressure gradient balances shear stress) and provide an analytical solution for tidally averaged along channel velocity. The scaling of this solution is in the form $u_e \sim \frac{1}{48}\frac{g}{\rho}\left(\beta\frac{\partial s}{\partial x}\right)\frac{H^3}{A_v}$. This scaling states that, when everything else is held constant, the estuarine exchange flow u_e (along channel subtidal flow) is proportional to the along channel salinity gradient $\frac{\partial s}{\partial x}$, inversely proportional to tidally averaged vertical eddy viscosity A_v and extremely sensitive to water depth H. Our recent work with current data collected in Newark Bay estuary at different channel depths shows that when along channel salinity gradient $\frac{\partial s}{\partial x}$ does not change significantly with channel deepening, the estuarine circulation u_e increases with H^3, which agrees with Hansen and Rattray (1965). However, the variation of A_v is not known in the Newark Bay estuary and therefore not able to account for in the analysis. In the Hudson River estuary where extensive field investigations have been conducted, Geyer et al (2000) showed that $\frac{\partial s}{\partial x}$ was relatively constant over the spring/neap cycle and u_e varied by a factor of 2~3. Chant et al (2007) later demonstrated that the vertical eddy viscosity varied by an order of magnitude over the spring/neap cycle in the Hudson. As a result, u_e should also vary by an order of magnitude rather than 2~3 times if the analytical solution applies, which was based on the simple momentum balance between the pressure gradient and vertical stress divergence. The fact that it did not

implied some missing dynamics, most likely the nonlinear advective terms. Following another line of investigation on the momentum budget, Trowbridge et al (1999) and Geyer et al (2000) introduced the momentum integral using the same momentum balance that Hansen & Rattray used for the analytical solution to calculate the stress profile. Surprisingly, the stress at the bottom compared very well with that from the quadratic drag law during neap tide, but not during spring tide when strong lateral advection was evident. Yet a simple model derived that neglected both advective acceleration and interfacial stress had good predictive skill. However, the fact that the analysis assumed zero interfacial stress begged the question—what was slowing down the surface layer? In addition, the fact that estimates of bottom stress from the momentum integral agreed with direct estimates made by eddy correlation during neap tides, but not during spring tides when lateral circulation was enhanced suggested that important dynamics may be missing from the Geyer et al (2000) analysis. Intrigued by this paradox, Lerczak et al (2004) studied the role of advection in the Hudson River estuary with an idealized numerical model and demonstrated that the advective terms were in fact of leading order in the along channel subtidal momentum budget, comparable to the pressure gradient and the vertical stress divergence terms. The question was raised as how Geyer et al (2000) managed to predict the estuarine exchange flow without any consideration of the advective terms. A few years later, the conundrum was solved by Scully et al (2009) through the use of a realistic model based of the Hudson River estuary. From the model he discovered a compensatory pair of forces, one being the advective acceleration and the other interfacial stress. Since the two forces were of similar strength yet opposing directions, they tended to cancel out in the momentum equation. This led to the fortuitous success of Geyer et al (2000) in estimating the exchange flow by ignoring both of them. Thus the nonlinear, advective acceleration terms have been of great interest in estuarine physics and because they have been studied extensively with models but not in the field, our goal is set to analyze their importance with data and to quantify their role in the momentum budget.

Data Description

The data we use in this study are primarily collected from moorings deployed in the lower part of the James River estuary (Figure 1). This estuary is located on the south side at the entrance of the Chesapeake Bay (magenta box in panel (a)). The experiment site (green box in panel (b) and (c)) is on the upstream of the James River Bridge and consists of two lines of moorings. The sea level data are taken from the NOAA (National Oceanic and Atmospheric Administration) tidal station at Sewells Point downstream of the moorings (panel (b)).

The moorings are placed along two lines cross the channel denoted as line 1 and line 2 (panel (c)). These two lines locate approximately 2.6 km and 1.4 km north of the James River Bridge respectively. Moorings along line 1 are labeled L1E, L1D, L1C, L1B and L1A starting from the south side of the channel (bottom left of panel (c)) to the north side of the channel. L1B is at the bottom of the main channel at depth around 10 m (panel (d)). L1A is at a slightly shallower region north of the main channel called 'the northern channel' in this paper. L1E, L1D and L1C are at the bottom of the southern slope referred to as 'the southern shoal'. Moorings along line 2 follow the same notation. The moorings along both lines are relatively evenly placed with an average spacing of around 0.5 km within each line and about 1.2 km between the two lines.

The mooring array consists of 10 Acoustic Doppler Current Profilers (ADCPs), 22 Conductivity and Temperature (CT) sensors and 4 Paroscientific pressure sensors which provide high precision pressure data (panel (d) and (e)). The ADCPs are fixed in the center of every mooring frame deployed to the bottom. Their vertical bin resolution is 0.25 m and their final data are every 30 minutes. The CT sensors are fixed to the chains hung by buoys over each mooring frame as well as on the legs of the frames. These CT sensors are fairly evenly distributed in the vertical to sample the entire water column. They cover most part of the transects with sampling frequency of 5 minutes. The Paroscientific pressure sensors are placed

along the B line (L1B and L2B) and the E line (L1E and L2E) on the mooring frames. They have a high accuracy (~1mm) and the B line sensors have a sampling frequency of 5 minutes while the E line sensors have a sampling frequency of 60 minutes.

The deployment lasted 40 days from 04/26/2010 to 06/05/2010 though some records were shorter due to bio-fouling (Figure 2) and the ADCP at L2D failed to get any data at all. The incomplete records include current data from L1B and L2B, salinity data from L2E, L2D at 6.7 m, L2C at 6.9 m, and L1D at 6.5 m. The rest covered almost the full length of the deployment.

Estuarine conditions

The estuarine conditions during these 40 days are shown in Figure 3. Daily river discharge data are from the combined stream flow data of USGS (U.S. Geological Survey) stations at Richmond, Matoaca and Providence. Tide (water level) data are from NOAA station at Sewells Point and wind data are from NDBC (National Data Buoy Center) Station DOMV2. The estuary received greater discharge after 05/14 compared to below 200 m^3/s before that. Tidal data shows one spring (tidal range greater than 0.76 m) and one neap (tidal range less than 0.76 m) over the period of a month. Valle-Levinson et al (2000) also noted this monthly (only one extreme spring and neap period per month), as opposed to fortnightly spring-neap variations in his study in the James. The tidally averaged water level displays slightly greater variation during the spring tide than during the neap. The wind data plotted in the last two panels are rotated to the along channel and cross channel directions according to the channel orientation. The positive direction in the along channel is downstream and in the cross channel is to the northeast. The winds are quite variable except for the period between 05/14 and 05/27 when both the along channel and the cross channel winds are weak. This will be studied later as the 'low wind spring tide' scenario. On the other hand, the along channel and cross channel winds reached maximum of 15 m/s and 11 m/s respectively on 05/06 and the along channel wind reached minimum of -9 m/s in the end of 05/09. These

are referred to the ‘high wind’ events and their influence will be discussed in both the flow field and the salt field.

Method

A right-handed coordinate system is applied with positive x (along channel) toward the ocean, positive y (cross channel) toward the northern channel (right side of the channel when looking into the estuary) and positive z (vertical) toward the water surface. Along x, the position of line1 is assigned to be 0 and line2 to be dx ($dx > 0$). All the data are interpolated according to a common time vector with 1 hour resolution. Subtidal variation is obtained through filtering the interpolated data with a cutoff frequency of 25 hours and window width of 50 hours.

Estimating the pressure gradient

Paroscientific pressure sensors are placed on the tripods (mooring frames) of L1B, L2B, L1E, L2E (Figure 1: panel (d-e)) and because the one at L1B experienced settling problems, the along channel pressure gradient is calculated from data at L1E and L2E, and the cross channel pressure gradient is calculated from data at L2B and L2E. Also, the lack of salinity data at the surface of L2E (Figure 1: panel (e)) and short record at the bottom of L2E (Figure 2) require us to get along channel baroclinic pressure gradient from the D line (L1D and L2D). Since the salinity record at the bottom of both L1D and L2D are short due to bio-fouling (Figure 2), only the data at surface and mid-depth are used.

Densities are calculated using the Equation of State $\rho = \rho(s, T, p)$ from salinity(s), temperature(T) and pressure(p) data of the CT sensors. They are then low-pass filtered to remove tidal and higher frequencies and also averaged vertically. The along channel baroclinic pressure gradient along the E line is calculated using the formula $(-g\frac{\partial \bar{\rho}}{\partial x}\overline{H})$. g is the gravitational acceleration and $\bar{\rho}$ is depth averaged, low-pass-filtered density along the D line and $\overline{H}$ is the mean water depth along the E line estimated from low-pass-filtered pressure data. The reason for the use of low-pass-filtered (subtidal) densities in the along

channel pressure gradient is that the original density data bring too much uncertainty to the pressure calculation on the tidal scale.

Barotropic pressure gradient along the E line is estimated with the pressure gradient from the Paroscientific sensors at L1E and L2E subtracted by the along channel baroclinic pressure gradient $-g\frac{\partial\bar{\rho}}{\partial x}\bar{H}$.

The pressure data for the cross channel direction is obtained from the Paroscientific sensors at L2B and L2E. Since there is only one CT sensor at the bottom of L2B (Figure 1: panel (e)). Depth averaged density for L2B is estimated from the average of densities at the bottom of L2B as well as the whole water columns of L2A and L2C. Depth averaged density for L2E is estimated from the top two levels of densities at L2D. The hydrostatic contributions to the pressures at L2B and L2E are calculated following the formula ($\bar{\rho}g\tilde{h}$). $\bar{\rho}$ is the estimated depth averaged density for that location and $\tilde{h}$ is the subtidal water depth inferred from the low-pass-filtered pressure record at that location. The cross channel barotropic pressure gradient is then calculated from the Paroscientific pressure data with their respective hydrostatic contribution removed.

According to the location and quality of salinity data, the cross channel transect is divided into 3 regions (Figure 1: panel (d-e)): the northern channel (A line—L1A and L2A), the southern channel (C line—L1C and L2C) and the southern shoal (D line—L1D and L2D).

Estimating the advective acceleration terms

The current data from the ADCPs are first rotated to u (along channel) and v(cross channel) velocities based on principle component analysis applied to each mooring individually. Then they are extrapolated to the surface with vertical shear linearly becoming zero toward the surface, as well as extrapolated to the bottom according to a logarithmic profile with velocity becoming zero at 0.01 m. The estimate of the full

advective term requires an estimate of the vertical velocity (w), which is too small to be reliably taken from the measurement of the ADCPs directly. Instead, it is calculated from u and v velocity profiles (including the extrapolated pieces) using the continuity equation (Eq.1).

$$\frac{du}{dx}+\frac{dv}{dy}+\frac{dw}{dz}=0$$
$$w=-\int_{z}^{0}\frac{du}{dx}dz-\int_{z}^{0}\frac{dv}{dy}dz \quad \text{(Eq.1)}$$

$$\bar{\rho}\left(\frac{\partial u}{\partial t}+u\frac{\partial \bar{u}}{\partial x}+v\frac{\partial u}{\partial y}+w\frac{\partial u}{\partial z}\right)=-\bar{\rho}g\frac{\partial \eta}{\partial x}-g\frac{\partial \bar{\rho}}{\partial x}z+\bar{\rho}fv+\frac{\partial \tau_x}{\partial z}$$
$$\bar{\rho}\left(\frac{\partial v}{\partial t}+u\frac{\partial \bar{v}}{\partial x}+v\frac{\partial v}{\partial y}+w\frac{\partial v}{\partial z}\right)=-\bar{\rho}g\frac{\partial \eta}{\partial y}-g\frac{\partial \bar{\rho}}{\partial y}z-\bar{\rho}fu+\frac{\partial \tau_y}{\partial z} \quad \text{(Eq.2)}$$

For the three advective acceleration terms on the left hand side of Eq.2, $\frac{\partial \bar{u}}{\partial x}$ and $\frac{\partial \bar{v}}{\partial x}$ are calculated from u and v averaged over the entire transect according to the area each mooring represents in order to reduce the influence of lateral variability entering into estimates of along-channel gradients; $\frac{\partial u}{\partial y}$ and $\frac{\partial v}{\partial y}$ are calculated from nearby moorings on the two sides of the mooring the calculation is based on whenever possible; $\frac{\partial u}{\partial z}$ and $\frac{\partial v}{\partial z}$ are calculated in the vertical with intervals at 0.25 m.

Eq.2 contains the momentum equations for both the along channel and cross channel directions, where $\bar{\rho}$ is the depth averaged density, f is Coriolis frequency and τ_x and τ_y are stresses at the along channel and cross channel directions respectively. The first term on the left hand side of Eq.2 is the local acceleration and the following 3 terms are field acceleration (advective acceleration) terms. The terms on the right hand side of Eq.2 are barotropic pressure gradient, baroclinic pressure gradient, Coriolis and vertical stress divergence.

In order to get a zero sum of momentum, the terms on the right hand side of Eq.2 are moved to the left hand side, as shown in Eq.3.

$$\bar{\rho}\left(\frac{\partial u}{\partial t}+u\frac{\partial \bar{u}}{\partial x}+v\frac{\partial u}{\partial y}+w\frac{\partial u}{\partial z}\right)+\bar{\rho}g\frac{\partial \eta}{\partial x}+g\frac{\partial \bar{\rho}}{\partial x}z-\bar{\rho}fv-\frac{\partial \tau_x}{\partial z}=0$$
$$\bar{\rho}\left(\frac{\partial v}{\partial t}+u\frac{\partial \bar{v}}{\partial x}+v\frac{\partial v}{\partial y}+w\frac{\partial v}{\partial z}\right)+\bar{\rho}g\frac{\partial \eta}{\partial y}+g\frac{\partial \bar{\rho}}{\partial y}z+\bar{\rho}fu-\frac{\partial \tau_y}{\partial z}=0 \quad \text{(Eq.3)}$$

Estimating vertical stresses

By integrating Eq.2 we can get the along channel and cross channel stresses (τ_{zx} and τ_{zy}) respectively (Eq.4). Surface stresses (τ_{sx} and τ_{sy}) are taken as wind stresses. ρ_{air} is the density of the air and u_w and v_w represent the along channel and cross channel winds respectively. The drag coefficient c_d (Eq.4) is determined following Large and Pond (1981) using wind speed measured at 10 m above sea level (u_{10}).

$$\tau_x^z=-\int_z^0\frac{\partial \tau_x}{\partial z}dz+\tau_x^s$$
$$\tau_y^z=-\int_z^0\frac{\partial \tau_y}{\partial z}dz+\tau_y^s$$
$$\tau_x^s=\rho_{air}c_d u_w^2 \quad \text{(Eq.4)}$$
$$\tau_y^s=\rho_{air}c_d v_w^2$$
$$c_d=\begin{cases}1.2\times10^{-3}, & 4\le u_{10}<11\\ (0.49+0.065u_{10})\times10^{-3}, & 11\le u_{10}<25\end{cases}$$

Results

Mean conditions

Mean subtidal flow

As observed by Valle-Levinson et al (2000) and others, the subtidal along channel flow (Figure 4) consists of two layers: the inflow in the lower layer restricted mostly to the main channel and the outflow in the upper layer over the southern shoal. In general, the averaged subtidal along channel flow (exchange flow) during the neap tide and during the spring tide only differ by a small degree. The incoming flow is more laterally sheared over the main channel during the spring and more vertically sheared during the neap. The upper layer is similar between spring and neap except that the vertical shear in the middle part of the transect is greater at neap, created by a lifted interface and greater incoming flow in the lower layer over L1C mooring.

A general pattern in the cross channel velocity field reveals a residual subtidal velocity from the northern side of the channel (right side in the figure) to the southern shoal (left side in the figure). The average magnitude of this southward velocity is about -0.01 m/s. This is caused by the asymmetry in lateral flows between the flood and ebb tide (Figure 5). This asymmetry in lateral flows is characterized by stronger near bottom flow during the flood (to the south) and stronger surface flows during the ebb (also to the south). Thus the tidally averaged lateral flow is to the south. Lerczak and Geyer (2004) also noted this in the modeling study of the Hudson River estuary and suggested that this asymmetry may lead to asymmetric sediment transport, further leading to asymmetric channel profiles. Moreover, this lateral flow acting on a tidally averaged salinity field implies a diapycnal mixing as it transfers salt from the main channel to the southern shoal.

Note that the lateral velocity is the weakest where the along channel velocity is the strongest (speed exceeding 0.1 m/s) on the subtidal scale, suggesting that the high velocities on the subtidal scale are mostly longitudinal.

Mean tidal flow

The mean tidal flow during both the spring and neap (Figure 5) shows very different magnitude (note that the color scales are different) compared to the mean subtidal flow. The average along channel velocities at both maximum flood and maximum ebb are greater during the spring than during the neap. Similar to the subtidal velocity structure, the center of flooding tide is more over the main channel during the neap while tilted toward the northern shoal during the spring. The ebb velocity during the spring displays similar pattern with that during the neap but with a greater magnitude.

In the cross channel direction, during spring and neap tidal conditions, the lateral circulation is reversed from maximum flood to maximum ebb. At maximum flood, the velocities in the upper layer and lower layer are comparable to each other but in opposite directions with slightly stronger southward flow in the lower layer. At maximum ebb, the velocities in the lower layer are considerably weaker than those in the upper layer resulting in excess flow to the south in the upper layer. This could be due to fluid from the wide northern flank flowing into the channel. On the subtidal scale the lateral circulation does not show dramatic difference between spring and neap tides although it is a bit stronger during the spring. This is different from what was described in the study of the Hudson River estuary by Lerczak and Geyer (2004) as well as Scully et al (2009), because the lateral flow at flood was much greater than that at ebb in the Hudson. Besides this, the lateral flow in the James shows a much 'clearer' structure than that in the Hudson with only the two-layer pattern in all these scenarios. The only exception is at the bottom of L1A during neap tide at maximum flood when the northward flow complicates the lateral velocity to 3 layers. Bear in mind that all these figures are showing the 'mean' condition of the specific scenarios.

Mean salinity field

The salinity data from the CT sensors do not have the same degree of spatial coverage as the velocity data do; however, after cautious interpolation among the available locations, a comprehensive salinity structure over the transect 1 is obtained and displayed in Figure 6. Transect 2 (not shown) carries the same feature. The tidal variation of the mean salinity can be observed from the horizontal panels as the left one is at the end of flood and the right one at the end of ebb. The subtidal variation can be seen from the vertical panels as the top one is during the spring tide and the bottom one is during the neap tide. Overall, the primary feature of the salinity field is less salty water over the southern shoal (spring) or surface (neap) and the saltiest water at the bottom of the main channel. The isohalines are more flat and dense during the neap tide and more tilted and sparse during the spring tide, indicating that the water column is more mixed during the spring. If tidally averaged, the salinity gradient will be directed toward the southern shoal (especially in the spring). Thus it will be in the same direction as the residual lateral flow which is also toward the south (Figure 4). Therefore the residual lateral flow would play an important role in the lateral mixing of the salinity.

Judging from the contours, there is greater tidal period variation during the spring. Within a tidal cycle in the spring (Figure 6: panels a and b), isohalines are relatively flat in the end of flood over the main channel but slope upwards to the north at the end of ebb. The vertical stratification is weaker at the end of flood and greater at the end of ebb. This is in agreement with MacCready and Geyer (2010) and indicates alternation between less stratified and stratified conditions, with maxima at the end of ebb (low tide). The source of this tidal fluctuation is from the relatively small tidal variation in the vicinity of the bottom of the main channel and great tidal period variation at the other stations toward the surface and the southern shoal.

Both vertical and lateral salinity gradients demonstrate tidal and subtidal variability. For the vertical gradient, when examined in the main channel, during spring tide, it is about 2 psu at the end of flood and

about 3.5 psu at the end of ebb. During neap tide, it is about 8 psu both at the end of flood and at the end of ebb. The spring-neap variation of the salinity gradient is stronger than the tidal variation even though the latter is also evident during the spring tide. For the lateral gradient, when examined at 4 m depth, during spring tide, it is about 1.5 psu at the end of flood and about 2.5 psu at the end of ebb. During neap tide, it is about 2 psu at the end of flood and about 4 psu at the end of ebb.

Therefore, stratification is more than 2 times stronger during neap than during spring and is enhanced from the end of flood to the end of ebb during the spring. Meanwhile, lateral salinity gradient is also strengthened from spring to neap and from the end of flood to the end of ebb.

Time series and the influence of wind

Time series of the subtidal flow

Apart from the mean conditions of the flow and salt field, the time series of these quantities are also explored, starting with the time series of the subtidal flow (exchange flow for the along channel and lateral flow for the cross channel) depicted in Figure 7. The two layers of the exchange flow in the upper panel and the two directions of the lateral flow in the lower panel share much variation due to the constraint of mass conservation.

And different from previous studies, the exchange flow does not show spring-neap variation while the lateral circulation does with stronger flow during the neap and weaker flow during the spring. This is in contrast with the field study by Lerczak and Geyer (2004) in the Hudson where the strength of the lateral circulation was slightly greater in the spring.

Moreover, in the upper panel, after 05/12, the out flow is apparently greater than the inflow probably due to the elevated river discharge (Figure 3). In the lower panel, the southward flow is consistently stronger than the northward flow, resulting in net transport of water to the southern shoal, echoing the residual southward velocities shown in Figure 4. The unusually immense inflow on 05/07 occurred one day after the high wind event (down estuary and northward: Figure 3) and came alongside the strongest southward flow in the lower panel. The strong lateral circulation and northward flow on 05/10 accompanied quite weak exchange flow in the along channel direction.

The magnitude of the temporal mean of the subtidal outflow and inflow are 643 and 620 m^3/s respectively calculated from Figure 7. The temporal mean of the river discharge yields 169 m^3/s from Figure 3. The temporal and spatial mean of the subtidal salinity gives 14 PSU for the upper layer and 18 PSU for the lower layer, introducing a stratification of 4 PSU between the two layers.

Knudsen (1900) provided a diagnostic solution for the exchange flow in steady state in terms of the stratification $Q_1 = \frac{s_2}{\Delta s} Q_R$ and $Q_2 = \frac{s_1}{\Delta s} Q_R$

where Q_R, Q_1 and Q_2 are the average of river discharge, upper layer flow (outflow) and lower layer flow (inflow) respectively. s_1 and s_2 are the average salinities of upper and lower layers and $\Delta s = s_2 - s_1$ is their difference.

Given the numbers above we get 761 m^3/s for the outgoing flow and 592 m^3/s for the incoming flow. The reason for our underestimated outflow may well be the fact that the integration of outflow over the velocity transect is missing section over the southern flank beyond the mooring array. Also, a bit more discharge from downstream of the gauges where we get the discharge data would certainly increase Q_R and thus both Q_1 and Q_2. Nevertheless, the good agreement between Knudson's relationship and our estimate of the inflow suggests that we have in fact captured the upriver transport associated with the estuarine exchange flow.

Time series of the subtidal density

The densities are calculated from the salinity, temperature and pressure data of the CT sensors. Apart from one sensor (L2C at 6.9 m) which can be represented by an adjacent one, densities from the rest of 21 sensors are low pass filtered and plotted in Figure 8. The IDs of the lines can be found in the legends and the locations of these sensors are shown in Figure 1 (panels d and e). The neap tide pieces are shaded and the wind events are indicated with the black arrows. The first thing we notice is that the density gradient during the spring (the non-shaded part) is more than 2 times weaker than that during the neap (shaded part). This is consistent with the mean salinity condition shown in Figure 6.

The second thing we notice is that there are distinctly two bodies of water: the surface water and the mid-depth/bottom water. Since the depth of the shallowest mid-depth sensor is 4.25m and the depth of the deepest surface sensor is 1.5m, it is implied that the interface between the two layers lies between 1.5m and 4.25m, above the middle of the water column. Thus the lower layer is thicker than the surface layer.

The two layers display very different temporal variation. During neap, the upper layer (solid lines) becomes lighter and the lower layer (dashed lines) becomes heavier, resulting in elevated density gradient. During the spring tide (non-shaded, middle part), due to the mixing of these water masses, the upper layer becomes heavier and the lower layer becomes lighter, producing a much weaker density gradient.

In the upper layer, the density usually decreases from the northern channel to the southern shoal, showing a clear cross channel density gradient. This was also observed by Valle-Levinson et al (2000) who stated that it was due to the influence of Coriolis acceleration. The same lateral gradient in salinity was also noted in Lerczak and Geyer (2004) in the Hudson. The gradient in the upper layer reached nearly zero after the upstream high wind event on 05/09 (Figure 3).

In the lower layer, the density decreases from the northern channel to the southern shoal as well as from bottom to mid-depth. The gradient is very clear during the neap. During the spring tide, the density at mid-depth of A is elevated above that at bottom of C along both lines from the tilting of isopycnals shown in Figure 6. This tilting of isopycnals is originated from the tilt of inflowing subtidal water in Figure 4 which brings to mid-depth of A denser water than the bottom of C. And during this period, the bottom of B and A and the mid-depth of A are well mixed with the heaviest water in the transect consistent with velocity structure in Figure 4.

For both transects, nearly 1 day after the strong down estuary wind on 05/06, the density started to increase from the heaviest part to the lightest part in the lower layer. It took the lower layer about 1.5 days to experience its influence. This is due to the augmented inflow after the high wind (Figure 7) which brought heavier water to the lower layer and diffused salt from the deepest part beyond. But this signal is trapped in the lower layer. Later nearly a day after the up estuary wind event on 05/09, the densities at all depths in the lower layer dropped altogether, more for the heavier part, and brought the density gradient to minimum both vertically and laterally. Besides being in the beginning of spring tide which could account for the reduction of the gradient, the reduction of the cross channel salinity gradient could also be explained as the up estuary wind brought lighter water from the south side to the north side through Ekman dynamics and served as a lateral mixing event for the water at all depth.

Therefore, the greatest density gradient is formed during the neap tide nearly one day after the strong down estuary wind and the least density gradient is formed during the spring tide nearly one day after the strong up estuary wind. Both times are marked by the tails of the arrows.

Influence of wind

It has been seen that the two high wind events (05/06 and 05/09: Figure 3) have a strong effect on not only the subtidal flow but also the subtidal density field and thus their influence is further explored by

checking the instantaneous response of the flow and salt field on the subtidal scale (Figure 9). The left column is during the strong down estuary wind (peak speed at 15 m/s) happened late in the day of 05/06. Panel (a) shows the flow condition at the time of the maximum wind; panel (c) shows the snap shot of transect 1 half day after the maximum wind when the southward flow, inflow and exchange flow all reached maximum; panel (e) is the snap shot of the salinity field when vertical salinity gradient reached its maximum 17 hours after the maximum wind. The right column is during the strong up estuary wind (peak speed at -9 m/s) that occurred around the end of 05/09. Panel (b) shows the flow condition at the time of the high wind; panel (d) shows the flow condition around this time when the northward flow reached its maximum and the exchange flow became very weak; panel (f) is a snap shot of the salinity field 8 hours after the high wind event.

During the strong down estuary wind in the end of 05/06 (a, c), the inflow was augmented to over -0.3 m/s compared to the -0.15 m/s in the mean condition (Figure 4) and the exchange flow reached the maximum (Figure 7). Through the Ekman dynamics, the down estuary wind brought the upper layer water to the south side of the transect, thus producing the maximum southward flow (c). The increased inflow elevated the salinity in the lower layer and created the maximum salinity gradient as shown in Figure 8. The vertical gradient is about 10 psu over the main channel, the strongest in the record. The lateral gradient is about 4 psu at 4 m depth, greater than usual.

During the strong up estuary wind in the end of 05/09 (b, d), the exchange flow was largely weakened and maximum northward flow was generated through the Ekman dynamics. The weakening of the exchange flow reduced the stratifying effect of the estuarine shear and allowed tidal and wind generated turbulence to mix the water column. Thus after the reduction in the exchange flow by the down estuary wind, the salinity in the lower layer as well as vertical stratification are reduced to be the minimum as shown in Figure 9.

Note that the max down estuary wind also happened toward the end of the first neap tide and the max up estuary wind came in the beginning of the second spring tide. Therefore, the vast difference between

the two columns not only show the influence of the along channel wind but also the spring-neap variation. From Figure 4 we learned that the exchange flow during neap is slightly greater than that during the spring and from Figure 6 we learned that the salinity gradient during neap is much greater than that during the spring. Therefore, the difference is a result of wind effect augmenting the spring-neap variation.

Also noteworthy is the structure of the along channel flow in that when it becomes very weak (b, d), it is more horizontally sheared as opposed to being vertically sheared. This is made possible by the weak stratification as shown in panel (f). Compared at the lower part of B mooring between these two wind events, we observe that the lateral flow is weak where the along channel flow reaches more than 0.2 m/s. This further testifies that the fastest flow is more possible to be longitudinal while the weak flow is more likely to have a greater lateral component.

Tidal period variation during low wind, spring tide

It has been shown that the high wind events have a significant influence on both the flow field and the salt field. In order to simplify the dynamics we choose the low wind time period for our further analysis. This time period happened to be in the spring tide from 05/13 to 05/27 (Figure 3). Discharge in this period ranged from about 150-300 m^3/s and both the along channel and cross channel winds were weak (less than 5 m/s) compared to the rest of the record.

The tide, flow and density conditions for this time period are plotted in Figure 10. Flood tide corresponds to high water level and ebb tide accompanies low water level (panel (a)). The density (panel (c)) is often in quadrature with the velocity so max density is usually in the end of flood and minimum density comes in the end of ebb. The three time series all show a relatively strong tidal cycle and a relatively weaker one during a period of one day before 05/17 and after 05/21. This semi-diurnal signal is more pronounced in

the tide and velocity time series as the density time series is complicated by a decreasing trend due to increasing discharge. What's more, the velocity time series (panel (b)) shows greater magnitude during flood than ebb and results in upstream flow on the subtidal scale (black line in panel (b)) at about -0.1 m/s, for this mooring lies in the region that is dominated by landward flows.

Tidal period variation of velocities

The vertical profiles of u, v and w are plotted in Figure 11 with blue, red and green lines respectively. u and v share the bottom axis with bounds between -0.7 m/s and 0.7 m/s. w is plotted against the top axis with green bounds between -0.0007 m/s and 0.0007 m/s. So w is 3 orders of magnitude smaller than u. In order to show the contribution of $\frac{\partial v}{\partial y}$ in the calculation of w, a partial w calculated using only $\frac{\partial v}{\partial y}$ is also plotted in the figure with red lines. The rows are for different locations and the columns are for different tidal phases.

The partial w is almost the same as w during the flood tide and apparently smaller than the full w during the ebb tide. This is because the flooding water is mainly coming in the main channel and does not have much variation along the x axis. However, the ebbing water is spread over the shoals and any increase in the shoal area (as from line 1 to line 2) would result in velocity difference in the longitudinal direction. Thus $\frac{\partial u}{\partial x}$ is negligible during the flood tide but significant during the ebb tide. But all of them present strong and clear tidal variation.

Except for L1A which is at the northern side of the main channel and very close to the northern flank, all the other locations have along channel velocity with great tidal asymmetry between flood and ebb. This asymmetry is displayed in stronger velocity at max ebb than at max flood as well as much greater velocity at the end of ebb than at the end of flood. This results in excess ebb velocity when averaged among tidal cycles.

The cross channel velocity shows a 2-layer structure at all the locations and its strength is relatively steady throughout much of the tidal phases. Except that at L1A, its structure and magnitude are similar within the flood tide as well as within the neap tide. During the flood tide, the southward velocity in the lower layer is greater than the northward velocity in the upper layer. During the ebb tide, the southward velocity in the upper layer is greater than the northward velocity in the lower layer. This results in southward velocity in both layers after taking tidal average.

The vertical velocity has a different story in that its overall magnitude tends to increase with water depth. For example, the magnitude of w is greatest at L1A, then at L1B and is the least at L1E. This could be explained by the fact that the vertical velocity has to go to zero at 0.01m above the bottom. Looking across all these locations we observe that during the flood, w is significant at L1B and L1A with negative value (going down) and its maximum is at the mid-depth. During the ebb, w is significant from L1D down to L1A with positive value (going up) and its maximum is at the surface. Its tidal asymmetry is therefore manifested in the structural difference between flood and ebb. So during the flood, water is going down mainly in the main channel with maximum value at mid-depth, implying convergence of horizontal velocities at the mid-depth during the flood; during the ebb, water is going up over most part of the transect with maximum value at the surface, implying divergence of horizontal velocities at the surface during ebb.

These characteristics are depicted in Figure 12 with the same color coding for velocities of the three directions. All three directions manifest tidal asymmetry in their spatial structures where max velocities are present in the mid-depth of the main channel at max flood while they are more spread to the surface of the southern shoal at max ebb. The cross channel velocity also manifests tidal asymmetry in magnitude as well as in layout for its southward portion is greater during the flood at mid-depth and during the ebb at the surface, thus further claiming the cause of the southward residual velocity after tidally average.

The momentum budget

As in the previous part, only the low wind, spring tide piece of data is used for the following analysis.

Along channel momentum budget

Method Validation

The along channel stress (τ_{zx}) is integrated from Eq.4 and the bottom stress (τ_x^b) is readily obtained by setting $z = -H$ in the integration of the momentum equation. Before starting the analysis of the momentum, this approach of using the momentum equation to get stress is validated between the comparison of the bottom stress from the momentum integration and the bottom stress from the quadratic drag law (using along channel velocity at the first bin as bottom velocity u_b). This relation is expressed in the following equation in which c_d is drag coefficient and $\bar{\rho}$ is depth averaged density.

$$\tau_x^b = c_d \bar{\rho} u_b |u_b|$$

The result (Figure 13) shows a good agreement indicating that this method is reliable. The correlation coefficients between these two estimates are 0.84, 0.75 and 0.8 for these 3 stations respectively. And the estimated c_d is around 0.003 for all the moorings, which matches the drag coefficient of 0.0031 from the regression analysis of the Hudson River (Geyer et al. 2000). The stress estimate for L1D and L1C are quite symmetrical between flood and ebb because these two sites are in the middle of the transect. For L1A, stress at flood tide is much greater than that at ebb because the center of the flooding water gets into the estuary through the main channel while the ebbing water flows out of the estuary over the southern shoal (Figure 5).

The estimated offset of the pressure gradient is determined from the linear regression analysis between these two ways for the estimate of bottom stress, chosen to bring the y intercept of the regression to zero following Geyer et al (2000).

The stress profiles

After the method is validated, the vertical profiles of the along channel stress can be obtained from the integration of Eq. 4. Their temporal mean profiles are shown in Figure 14 in the low wind period under different tidal conditions. At the very surface, the stress is only from wind, therefore quite small. Since it is integrated with z, its magnitude increases with depth and reaches maximum at the bottom. Its direction is consistent with the depth averaged flow in that stress is negative (upstream) during flood and positive (downstream) during ebb. Except for the end of flood at L1C, stress is weaker at the slack tide than at max flood/ebb. This is because the momentum is greater at max flood/ebb than at the slack tide. Between flood and ebb, the stress becomes more symmetric at depth. In the top layer, it is greater at the southern side of the channel (L1D and L1C) during ebb and at the northern side of the channel during flood. This is also consistent with the structure of the tidal flow in Figure 11.

Subtidal momentum budget

In order to quantify the importance of the advective acceleration terms, we calculate and plot all the terms in the momentum equation (Eq.3). The low pass filtered momentum terms from Eq.3 are averaged over the low wind, spring tide piece in Figure 15.

From panels (A, B, C), local acceleration ($\bar{\rho}\frac{\partial u}{\partial t}$) and negative Coriolis force ($-\bar{\rho}fv$) are nearly 0 after tidal average due to their tidal variation. This is consistent with the findings of Lerczak and Geyer (2004).

Negative baroclinic pressure gradient ($g\frac{\partial \overline{\rho}}{\partial x}z$) increases linearly with depth because it is calculated from depth averaged, low-pass-filtered density gradient. The reason we use low pass filtered density is that the original density data introduces too much high frequency uncertainty. It reaches around 0.02 ($\frac{kg}{m^3}\times\frac{m}{s^2}$) (also Newton per unit volume) at the bottom, indicating a subtidal baroclinic pressure gradient of about -0.02 (N/m^3) upstream. This is in comparison with the downstream set barotropic pressure gradient of 0.006 (N/m^3) throughout the water column.

The next leading term is the along channel advective acceleration term $\bar{\rho}u\frac{\partial \overline{u}}{\partial x}$ which is significant at L1D (A) and L1C (B) in most part of the water column. At L1A, the advective acceleration is to a large degree represented by the $\bar{\rho}v\frac{\partial u}{\partial y}$ term, especially in the top layer above -4m. The other term $\bar{\rho}w\frac{\partial u}{\partial z}$ is also clearly taking a role at all 3 locations (A, B, C). To simplify the budget, we combine the three advective acceleration terms as one and the pressure gradient terms as one (D, E, F) and plot with dashed lines. In the very top layer (above -2 m for L1D and L1C and above -3 m for L1A), $-\frac{\partial \tau_x}{\partial z}$ is mainly balanced by the advective acceleration terms and modified by the pressure gradient terms. The advective acceleration becomes almost zero when the pressure gradient changes sign, at about -2 m for L1D and L1C and about -3 m for L1A. This marks the base of the top layer.

In the bottom layer (below -5 m for all three locations), the advective acceleration becomes weaker and decreases toward zero. $-\frac{\partial \tau_x}{\partial z}$ is mostly balanced by the pressure gradient and influenced by the advective acceleration terms. Here is where it comes closest to the classic theory proposed by Pritchard (1956), whereas his theory applied to the whole water column. The advective acceleration at L1D and L1C are similar (D, E) in that it is negative and reaches max magnitude at -1m and disappears at the base of the top layer as well as at the base of the bottom layer. The advective acceleration at L1A is different as it is positive in most of the top layer and bottom layer and becomes negative only in the middle layer. And it

does not show a subsurface maximum at about -1 m. This is because the major advective acceleration term for L1A $\bar{\rho}v\frac{\partial u}{\partial y}$ is positive, as is evident from Figure 4.

The middle layer is the most complex because it is the transition place where the advective acceleration ceases to be dominant and the pressure gradient starts to gain more significance with depth.

Note that in order to get a zero sum, all the momentum terms plotted in this study are from Eq.3, which means that the forces may have a different sign from their regular format. For instance, at L1D and L1C, the stress divergence ($\frac{\partial \tau_x}{\partial z}$) is positive ($-\frac{\partial \tau_x}{\partial z}$, the one in the plot, is negative) and slows down the landward residual flow in the lower layer. It is negative and slows down the ocean ward residual flow in the upper layer. At L1A, it is positive most of the time except for the middle layer and acts to slow down the landward residual flow in the whole water column. This is strictly consistent with the subtidal along channel flow structure seen in Figure 4 as the whole water column at L1A is landward flow.

On the subtidal scale, since the advective acceleration terms are negative (positive if moved to the right hand side of Eq.3) at L1D/L1C and positive at L1A, they would accelerate the along channel flow seaward at the surface of L1C/L1D sites and landward at the surface of L1A site. Because the residual flow is going seaward at L1C/L1D and landward at L1A (Figure 4: upper panel) in the spring, advection certainly strengthens the structure of the along channel subtidal flow, i.e. it augments the exchange flow.

Tidal momentum budget

For the tidal scale, we use the information from Figure 10 and group the data into four categories: max flood, end of flood, max ebb and end of ebb. The average is taken from each group and plotted in Figure 16. Local acceleration ($\bar{\rho}\frac{\partial u}{\partial t}$) is in quadrature with u and displays clear tidal variation with max magnitude at the end of flood/ebb. Also tidally variable term is $-\bar{\rho}fv$ which is essentially the shape of v with a

negative sign. The negative barotropic pressure gradient ($\bar{\rho} g \frac{\partial \eta}{\partial x}$) also fluctuates within the tidal cycle and that is why its tidally averaged value is fairly small (Figure 15). The negative baroclinic pressure gradient ($g \frac{\partial \bar{\rho}}{\partial x} z$) is relatively invariable throughout the tidal cycle as it is calculated from the tidally averaged salinity data (the original salinity data brings too much high frequency uncertainty).

The along channel advective acceleration term $\bar{\rho} u \frac{\partial \bar{u}}{\partial x}$ is only significant during the ebb and is similar at L1D and L1C. At L1A it becomes much weaker especially at the end of ebb caused by a small u (Figure 11). Because u is positive during ebb, the negative $\bar{\rho} u \frac{\partial \bar{u}}{\partial x}$ indicates negative $\frac{\partial \bar{u}}{\partial x}$ during this time period. This means that during the ebb tide, the along channel velocity decreases toward the head of the estuary probably due to the increase in the shoal area. This can also be inferred from the difference between the partial w and the full w shown in Figure 11.

The cross channel advective term $\bar{\rho} v \frac{\partial u}{\partial y}$ is only important at L1A from the end of flood all the way to the end of ebb. It is a leading term at max ebb especially in the surface layer as it almost balances the negative barotropic pressure gradient. After examining Figure 5, we understand that $\bar{\rho} v \frac{\partial u}{\partial y}$ is only effective during the ebb tide when there are both large cross channel velocity v and lateral shear in the along channel velocity $\frac{\partial u}{\partial y}$.

The vertical advective acceleration term $\bar{\rho} w \frac{\partial u}{\partial z}$ becomes important around the end of ebb at L1D and L1C as well as during the flood at L1A. Its magnitude is mainly determined by the vertical gradient of the along channel velocity $\frac{\partial u}{\partial z}$ as seen from Figure 5.

$-\frac{\partial \tau_x}{\partial z}$ is calculated from the balance with the sum of all the other terms. It shows a clear tidal variation as it is mostly negative during the flood and positive during the ebb. Note that the stress divergence ($\frac{\partial \tau_x}{\partial z}$: friction) will be positive during the flood and negative during the ebb. Therefore as commonly understood, it would reduce the incoming flow during the flood and the outgoing flow during the ebb.

As we did with the subtidal momentum budget, Figure 17 combine the three advective acceleration terms as one and the pressure gradient terms as one. These are plotted with thick dashed lines. A glance of Figure 17 reveals why the advective acceleration becomes so important on the subtidal scale: it does not cancel out over the tidal cycle. It is insignificant during the flood tide except for L1A where it accelerates the along channel flow seaward at the end of flood. And during the ebb tide, it accelerates the along channel flow seaward at both L1D and L1C and accelerates the flow landward at L1A. Therefore, during the ebb tide, it tends to speed up the flow on the south side of the channel and slow down the flow on the north side of the channel. This is equivalent to superimposing the residual circulation on the tidal flow during the ebb. And since the max of the along channel velocity is at the south side, it would tend to increase the lateral gradient of the along channel flow during ebb.

To conclude, the advective acceleration is significant in all three regions between maximum ebb tide and the end of ebb tide. It accelerates along channel flow landward over the northern channel and seaward over the southern shoal, thus would reduce the speed over the northern side and increase it over the southern side. From the regression analysis in Geyer et al (2000), a linear relationship between the momentum integral estimate and drag coefficient estimate was satisfied during the flooding tide but disproved at the maximum ebb with excessive estimate of stress from the momentum integral. Since the advection was not included in the momentum equation used in this study, it can be inferred that the advection may have served as a momentum sink which tampers the integrated stress to a more realistic value. Whether being a sink or a source, the role of the advection has to be determined from its location. As for L1A (near the main channel) during the max ebb, including the advection terms would decrease $-\frac{\partial \tau_x}{\partial z}$ at the surface as well as the bottom stress integrated from it (Figure 14: green line in panel L1A). Therefore from what we have observed in the momentum budget, the advective acceleration may well have served as the momentum sink during the ebb tide in the Hudson.

Cross channel momentum budget

After discussing the along channel momentum budget we also examined the cross channel using the same approach. The momentum terms are calculated from Eq.3 and their low pass filtered values are plotted in Figure 18. Depth averaged density increases down slope of the southern shoal (Figure 6) and results in positive $\frac{\partial \bar{\rho}}{\partial y}$ at L1D and L1C. Compared to the along channel, $\bar{\rho} g \frac{\partial \eta}{\partial y}$ is about 3 times greater than $\bar{\rho} g \frac{\partial \eta}{\partial x}$, and $g \frac{\partial \bar{\rho}}{\partial y} z$ is about 5 times greater than $g \frac{\partial \bar{\rho}}{\partial x} z$. And the first order balance is between pressure gradient (baroclinic and barotropic combined) and friction.

At the tidal scale (Figure 19), $g \frac{\partial \bar{\rho}}{\partial y} z$ changes slightly with the tidal cycle. It is very weak at L1A except for the end of ebb scenario. $\bar{\rho} g \frac{\partial \eta}{\partial y}$ displays tidal asymmetry in that the negative value during the ebb tide is greater than the positive value during the flood tide. This is the source of negative $\bar{\rho} g \frac{\partial \eta}{\partial y}$ in the subtidal momentum budget. $\bar{\rho} \frac{\partial v}{\partial t}$, $\bar{\rho} v \frac{\partial v}{\partial y}$and $\bar{\rho} w \frac{\partial v}{\partial z}$ are noticeable at some tidal phases but the dominant terms are pressure gradient, friction and Coriolis. This is simply an Ekman balance and agrees with findings in Scully et al (2009) who commented that Ekman transport is the driving dynamics in the bottom boundary layer. Since his lateral flow had a zero cross-channel average the mechanism also applied to the whole water column. On the other hand, this is consistent with the findings of Valle-Levinson et al (2000) in the statement that 'the transverse dynamics of a partially stratified estuary (the James River estuary) are far from being in geostrophic balance.'

Discussion

Advection seen in the along channel momentum budget

Two questions are raised from the along channel momentum budget. The first one is: Why are the advective acceleration terms important between maximum ebb and the end of ebb? And the second one is: Why is their sum negative over the southern shoal and positive at the northern channel?

To answer the first question, we need to go back to Figure 16 where it shows that $\bar{\rho}u\frac{\partial \bar{u}}{\partial x}$ is negative during the ebb tide. Since u is positive during ebb based on our definition, $\frac{\partial \bar{u}}{\partial x}$ needs to be negative which means that $\bar{u}$ decreases from line 1 to line 2. This could have been caused by the increase in shoal area from line 1 to line 2. It also implies a larger transect area at line 2 and divergence from line 1 to line 2. It is not significant during flood because the along channel tidal velocity is asymmetric. The major (high velocity) part of the flooding water is in the main channel and is relatively insensitive to the change in shoal area. On the other hand, the high velocity during ebb is at the surface over the southern shoal and thus very sensitive to the increase of the shoal area.

And from Figure 5 (upper right panel), the only time and place where $\bar{\rho}v\frac{\partial u}{\partial y}$ could be significant is during ebb tide at mooring L1A because $\frac{\partial u}{\partial y}$ is the greatest and v goes right cross the gradient. Here low momentum fluid from the flank is advected onto the main channel during ebb which essentially accelerates the flow in the main channel landward, thus augmenting the exchange flow. In other cases, v and $\frac{\partial u}{\partial y}$ are frequently aligned and thus $\bar{\rho}v\frac{\partial u}{\partial y}$ does not transfer momentum efficiently.

The above explains why the advective acceleration terms are important during the ebb tide rather than during the flood tide. We still cannot determine why it is the second half of the ebb tide in particular.

The second question can also be answered and understood from the above discussion. The negative sign of $\bar{\rho}u\frac{\partial\bar{u}}{\partial x}$ is defined by the channel geometry between line 1 and line 2 as when u is positive, $\frac{\partial\bar{u}}{\partial x}$ is negative. The positive sign of $\bar{\rho}v\frac{\partial u}{\partial y}$ is determined by the velocity structure during the ebb tide in transect 1 as shown in Figure 5 where v is negative and $\frac{\partial u}{\partial y}$ is also negative in the surface layer (upper right panel in Figure 5).

Advection seen in the salt field

The role of lateral advection is also seen in the salinity field from Figure 20, which shows the temporal mean of maximum salinity minus minimum salinity over the whole record. The numbers represent the scope of tidal fluctuation of salinity at specific locations. The average tidal variation of salinity over the 2 transects is around 2.5 psu. However, at the bottom of the northern channel the tidal fluctuation is only around 0.5 psu due to supply of fresh water during flood and salty water during ebb through advection. Vice versa, at the bottom of the southern shoal, the greater tidal fluctuation confirms advection of salty water during flood and fresh water during ebb, as indicated in Figure 5.

Summary

This extensive dataset has allowed us to undertake analysis not possible otherwise, leading to quite a few interesting results, in spite of some missing records. Among these are the estimate of barotropic pressure gradient with the aid of the Paroscientific sensors, the estimate of the advective terms with instruments sophisticated lined up over two transects as well as the estimate of vertical velocity.

The estuarine conditions are ideal in that we have both higher discharge and lower discharge scenarios, spring tide and neap tide, and above all, high wind period and low wind period, which enable us to experimentally explore the effect of winds on the flow and salt field.

Different from what we expected, there is not a clear spring-neap variation for the exchange flow but the lateral flow varied over the spring-neap cycle with greater flow during neap and weaker flow during the spring. Also on the subtidal scale is the persistent southward flow cross the transect caused by the excess of southward velocity in the lateral circulation. This corresponds well with Lerczak and Geyer (2004) as Lerczak also noticed that the advective term persists after averaging over a tidal cycle because of the asymmetry in the strength of the lateral flow between flood and ebb. We note that this study is the first to provide a detailed analysis of advective accelerations in estuaries based on field measurements.

On the tidal scale, far from what was observed in Lerczak and Geyer (2004), the strength of lateral circulation at ebb tide is comparable to that at flood tide, even though it reverses direction between flood and ebb. It is similar within flood and ebb both in structure and strength.

The vertical velocity is 3 orders of magnitude smaller than the along channel velocity and displays clear tidal variation due to change in horizontal flow divergence and convergence. During flood, water is going down mainly in the main channel with maximum value at mid-depth; during ebb, water is going up over most part of the transect with maximum value at the surface. The partial w calculated using only $\frac{\partial v}{\partial y}$

reveals that $\frac{\partial u}{\partial x}$ is negligible during the flood yet plays a significant role during the ebb. This is further confirmed in the along channel momentum budget on the tidal scale.

The salinity (density) increases from the southern shoal toward the main channel as well as from surface to the depth. There is a clear two layer structure from the salinity time series. In the salinity field, stratification is more than 2 times stronger during neap than during spring and is enhanced from the end of flood to the end of ebb during the spring. Meanwhile, lateral salinity gradient is also strengthened from spring to neap and from the end of flood to the end of ebb.

After the strong down estuary wind in the end of neap, the inflow and exchange flow reached its maximum and through Ekman dynamics, the southward flow in the cross channel direction also reached maximum. The increased inflow elevated the salinity in the lower layer and created the maximum salinity gradient. After the strong up estuary wind in the beginning of spring, the exchange flow was largely weakened and maximum northward flow was generated through Ekman dynamics. With the weakening of the exchange flow after the maximum down estuary wind and the onset of the northward flow, the salinity in the lower layer was reduced to be the minimum. Therefore, the greatest density gradient is formed during the neap tide nearly one day after the strong down estuary wind and the least density gradient is formed during the spring tide nearly one day after the strong up estuary wind.

The stress integral works well as a way to estimate vertical stress based on the comparison between the integrated bottom stress and that calculated from the drag law. The drag coefficient c_d is estimated to be around 0.003.

On the subtidal scale during the low wind, spring tide period, the first order along channel momentum balance is between stress divergence and advection, revised slightly by pressure gradient in the top layer. In the bottom layer, the first order balance is between stress divergence and pressure gradient, modulated by advection. This testifies that it is problematic to use the classic momentum balance between stress divergence and pressure gradient in the James River estuary except for the bottom layer.

Advection accelerates the along channel flow seaward over the southern shoal and landward over the northern channel and would augment the residual flow.

On the tidal scale, advection is not canceled out during a tidal cycle and becomes a leading order term between maximum ebb and the end of ebb at the surface. It accelerates along channel flow seaward over the southern shoal and landward over the northern channel, thus would increase the along channel velocity over the southern shoal and decrease it over the northern channel. This is equivalent to adding more subtidal flow to the tidal scale. Therefore, the effect of the advection terms on tidal scale is the same as that on the subtidal scale since advection is only prevalent during the ebb tide.

The momentum balance for the cross channel direction is between pressure gradient (baroclinic and barotropic) and stress divergence on the subtidal scale. And on the tidal scale, the leading terms are pressure gradient, Coriolis and stress divergence. The balance is also known as Ekman dynamics and thus the lateral circulation is driven by the earth's rotation.

The influence of momentum advection is also clearly seen in the salinity field as it increases the tidal fluctuation of salinity over the southern shoal and reduces it over the main channel.

Figures

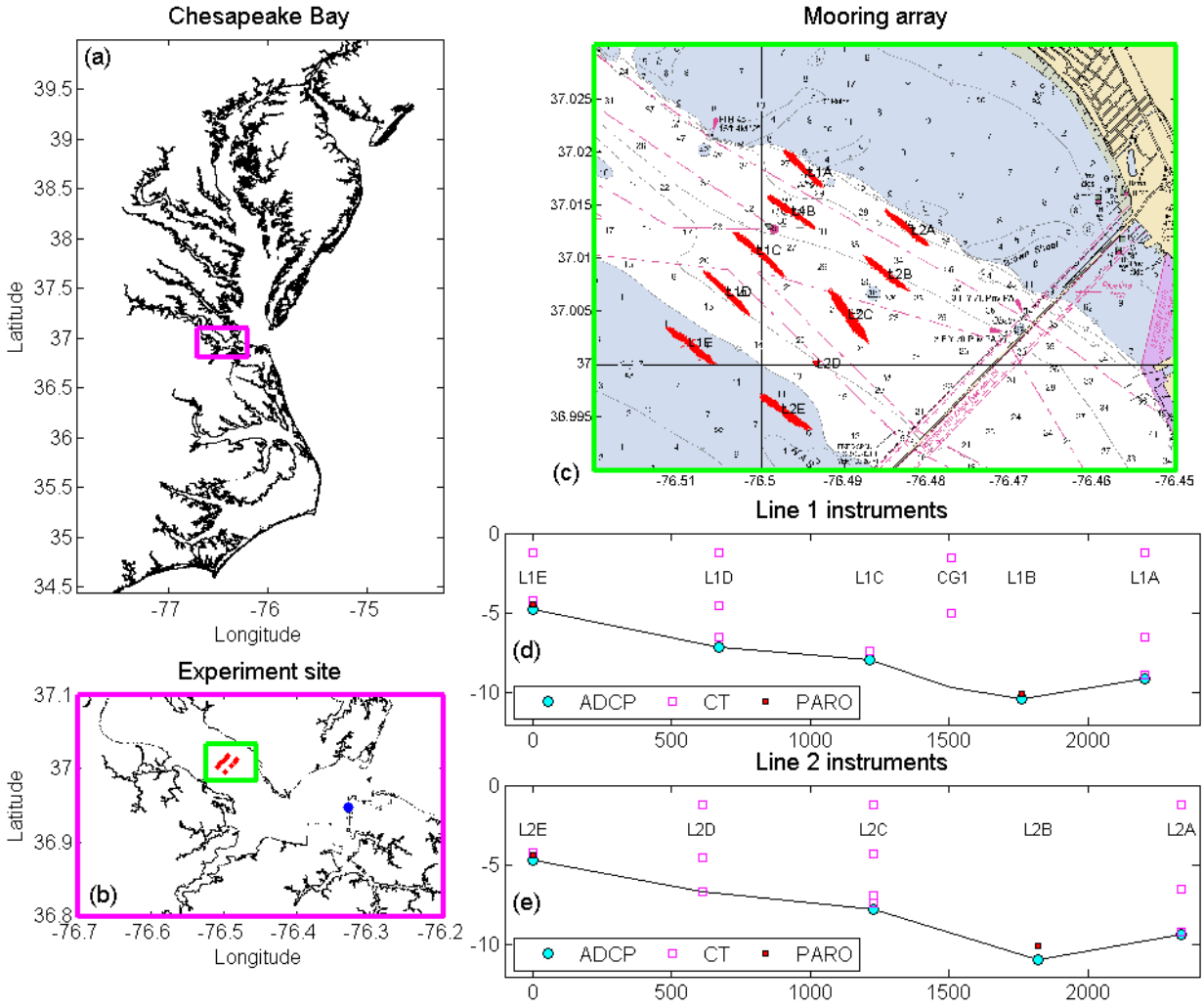

Figure 1: The James River estuary and field instrument locations. (a): The James River estuary in the context of Chesapeake Bay. The magenta rectangle marks the area of the lower estuary. (b): Map of the experiment site. The red dots show the locations of the moorings and the green rectangle marks the area of the mooring array. The blue dot indicates the location of NOAA tidal station at Sewells Point. (c): The mooring array in 2 lines with red clustered arrows showing surface velocity. The light blue shaded area indicates the shallow shoals. The James River Bridge is shown in the lower right of the chart. (d-e): Locations of 3 types of instruments deployed along the 2 lines. X-axis is the distance from the E mooring with unit 'm' and y-axis is depth below the surface also with unit 'm'. A line (L1A-L2A) is referred to the northern channel, B line (L1B-L2B) is referred to the main channel and the C, D, and E lines are referred to the southern shoal in this paper.

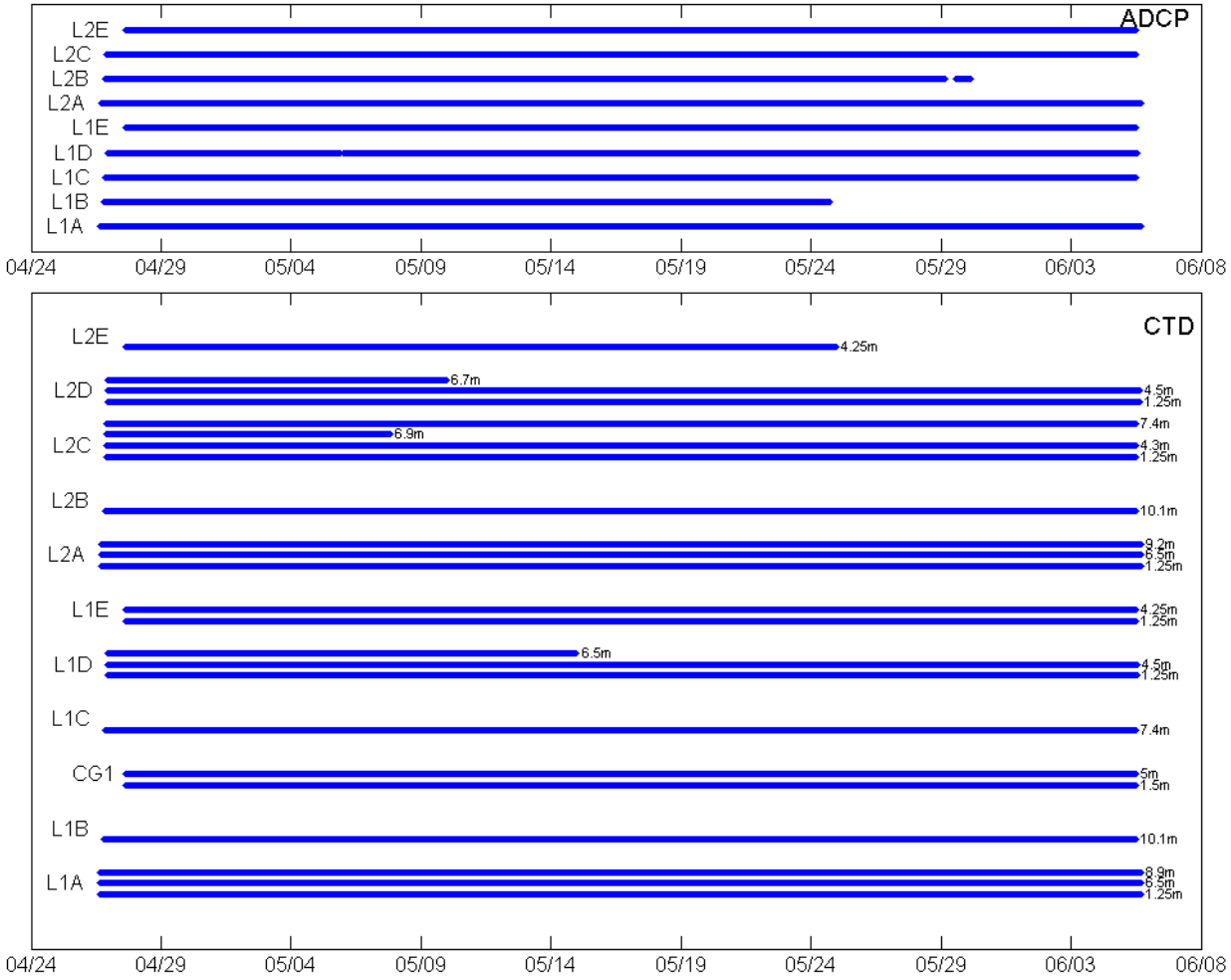

Figure 2: Duration of field data from ADCP and CTD sensors. Upper panel shows the duration of ADCP data with instrument locations labeled on the left; lower panel shows the duration of CTD data with sensor locations labeled on the left and sensor depths (below surface) indicated on the right.

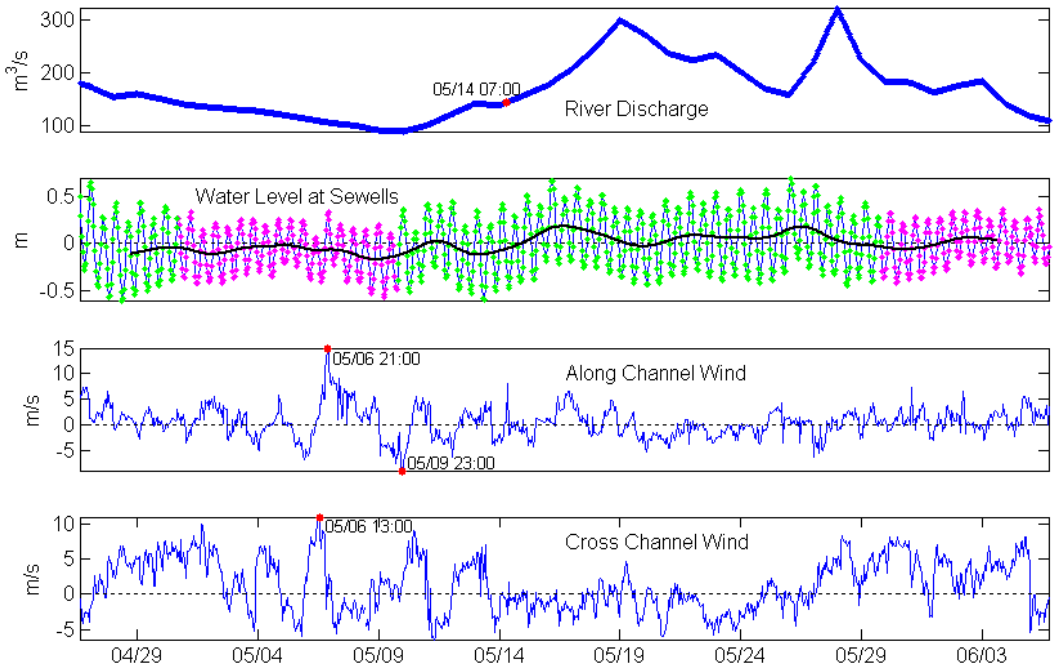

Figure 3: Time series showing estuarine conditions during the experiment period. The top panel is the river discharge and the red dot marks the time when the discharge started to increase. The second panel shows water level at Sewells Point with the green dots indicating spring tide and the magenta dots indicating neap tide. The black line is the tidally averaged water level. The lower two panels show the time series of winds and the red dots denote times of extreme winds. Positive direction is downstream for along channel wind and northward for cross channel wind.

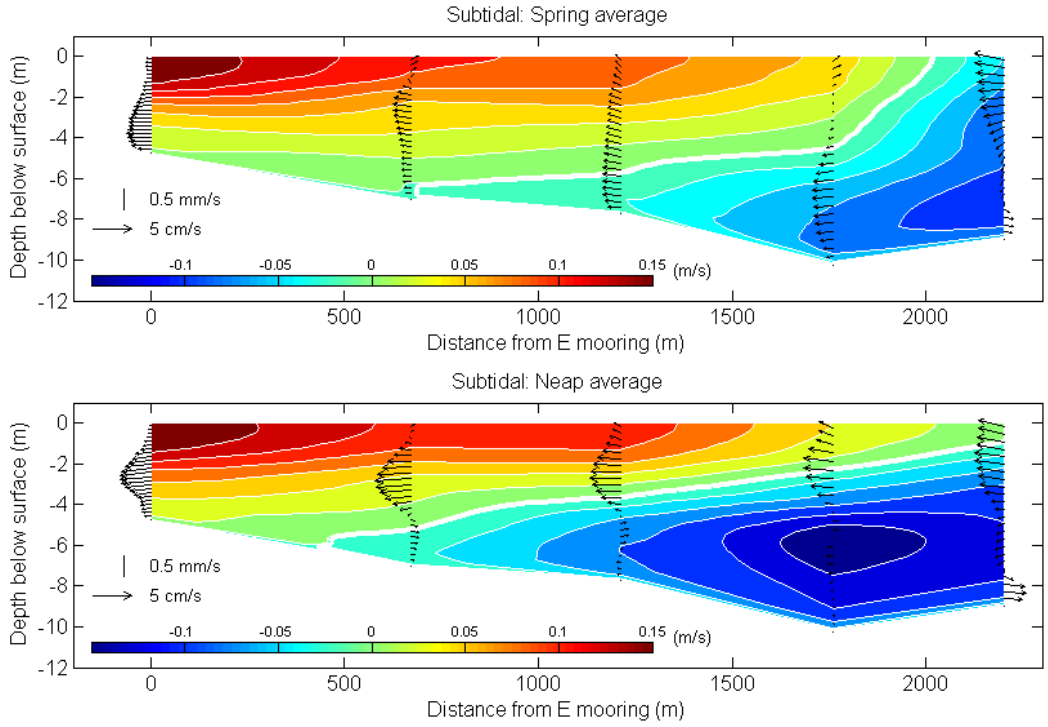

Figure 4: The average conditions of subtidal velocities over transect 1 (looking into the estuary). The color filled contours describe along channel velocities and the vectors scale with the across channel velocities. The thick white lines indicate zero along channel velocity. The along channel, across channel and vertical velocities are in different units as shown in the figure.

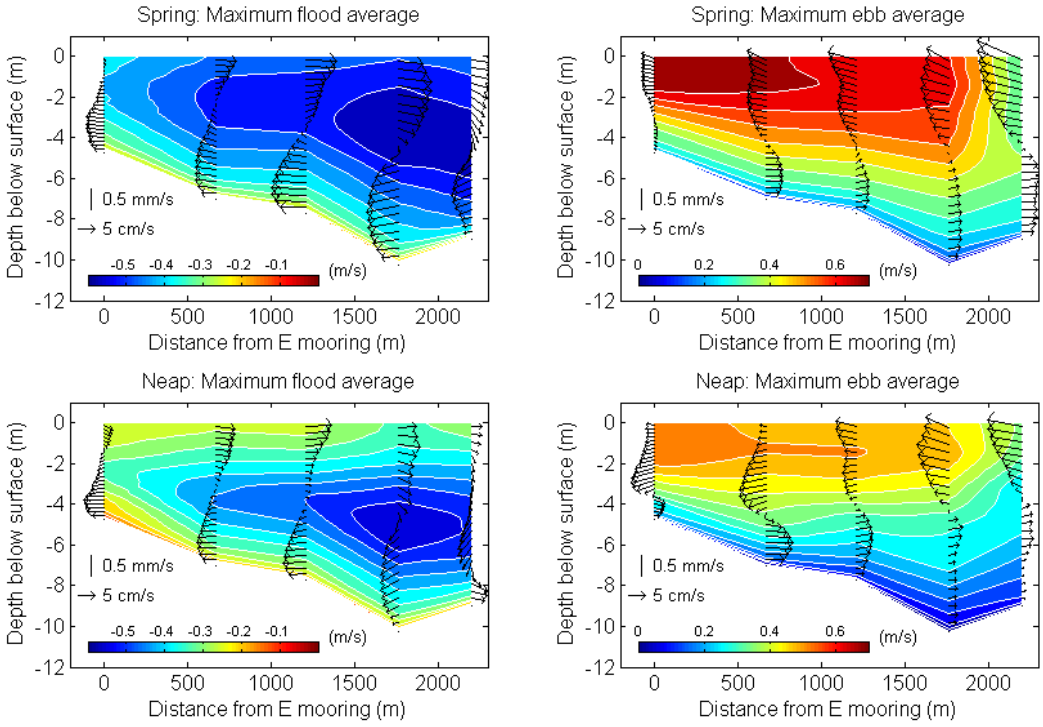

Figure 5: The average conditions of velocities over transect 1 (looking into the estuary) at the maximum flood and ebb tide. The color filled contours describe along channel velocities and the vectors scale with the across channel velocities. The along channel, across channel and vertical velocities are in different units as shown in the figure. Note that the color bars have different ranges between maximum flood and ebb for the along channel velocity.

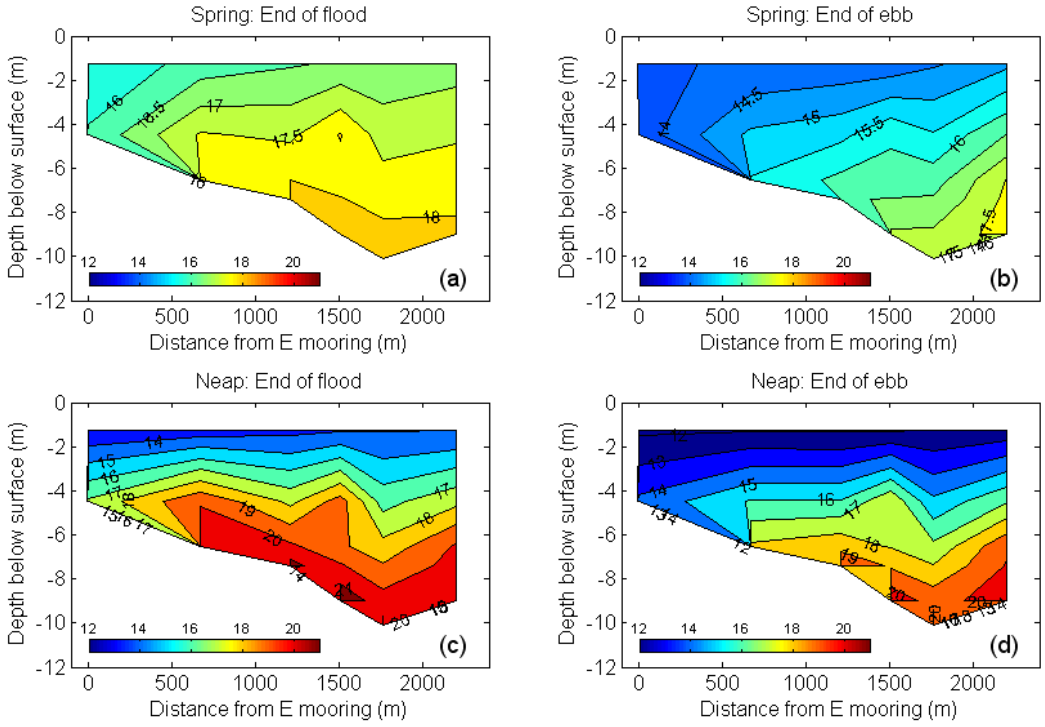

Figure 6: Interpolated salinity plot for transect 1. Every panel shows the temporal average of salinity during the tidal condition indicated in its individual title. Contours are in the unit of psu and color bars have the same range from 12 psu to 21 psu. Note that panel (a) and (b) are contoured every 0.5 psu while panel (c) and (d) are contoured every 1 psu.

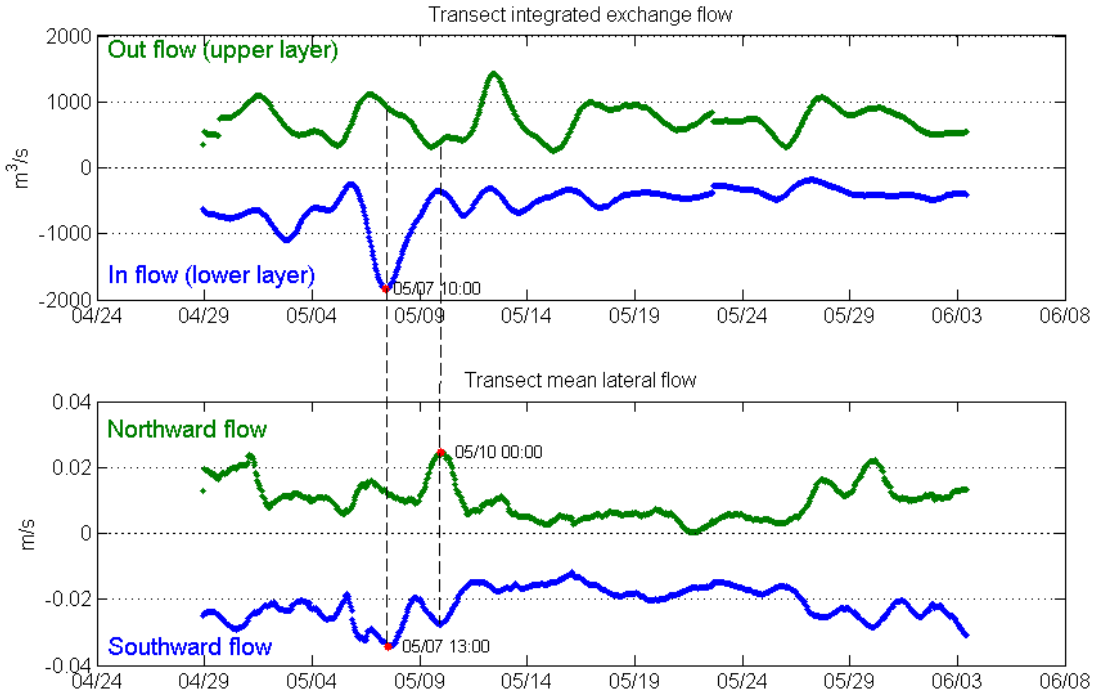

Figure 7: Time series of along channel and across channel subtidal flow. In the upper panel, along channel flow (exchange flow) was integrated over transect 1 with subtidal velocities from ADCPs L1E, L1D, L1C, L1B and L1A. Positive is out flow from the estuary in the upper layer and negative is in flow to the estuary in the lower layer. The lateral circulation is shown in the lower panel with northward flow and southward flow both averaged over transect 1. The red dots indicate time of extreme flows and the dashed lines show the flow magnitude in all directions during these times. Time stamps when the extreme flow occurred are also provided.

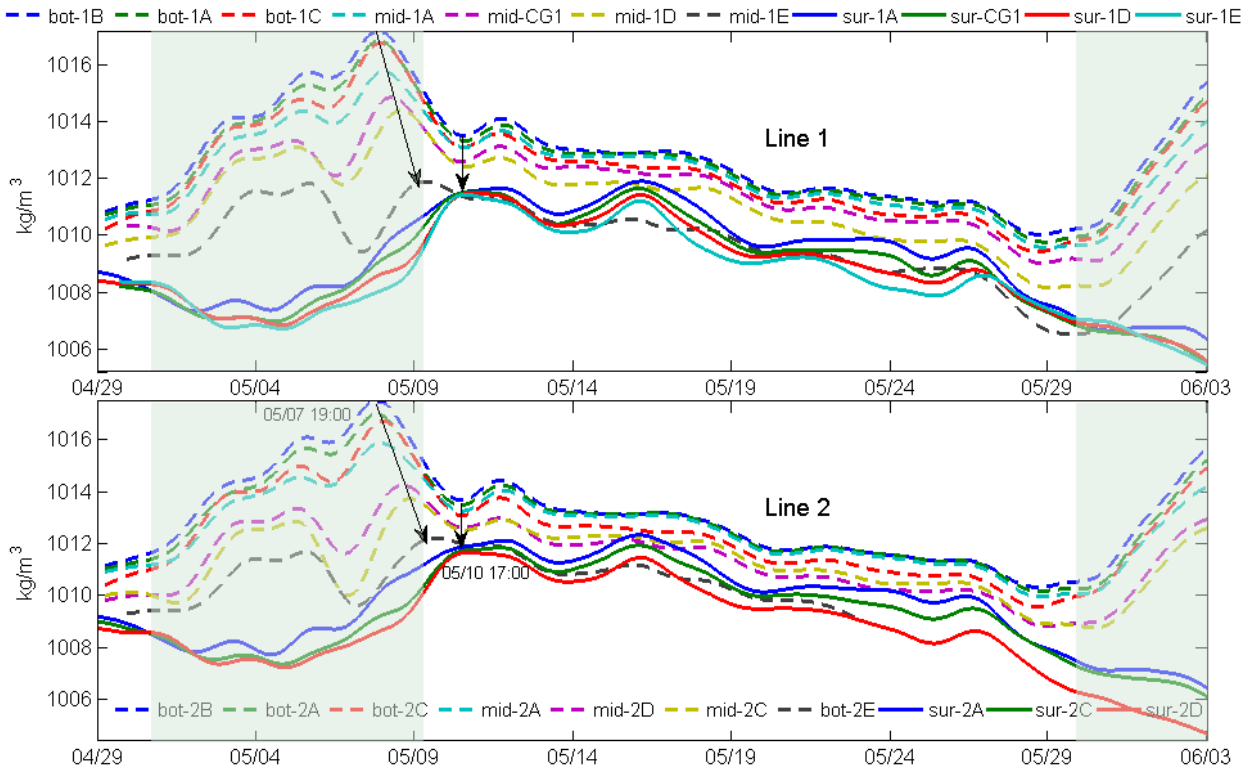

Figure 8: Time series of subtidal densities from all the CTD sensors along the two lines (see Figure 1 for instruments layout). Legend for line 1 is on top of the figure; legend for line 2 is in the bottom panel. Shaded areas are during neap tides. The start time of the longer arrows and time of the shorter arrows are shown in the lower panel. All solid lines are time series of surface densities and dashed lines are densities from the bottom and mid-depth.

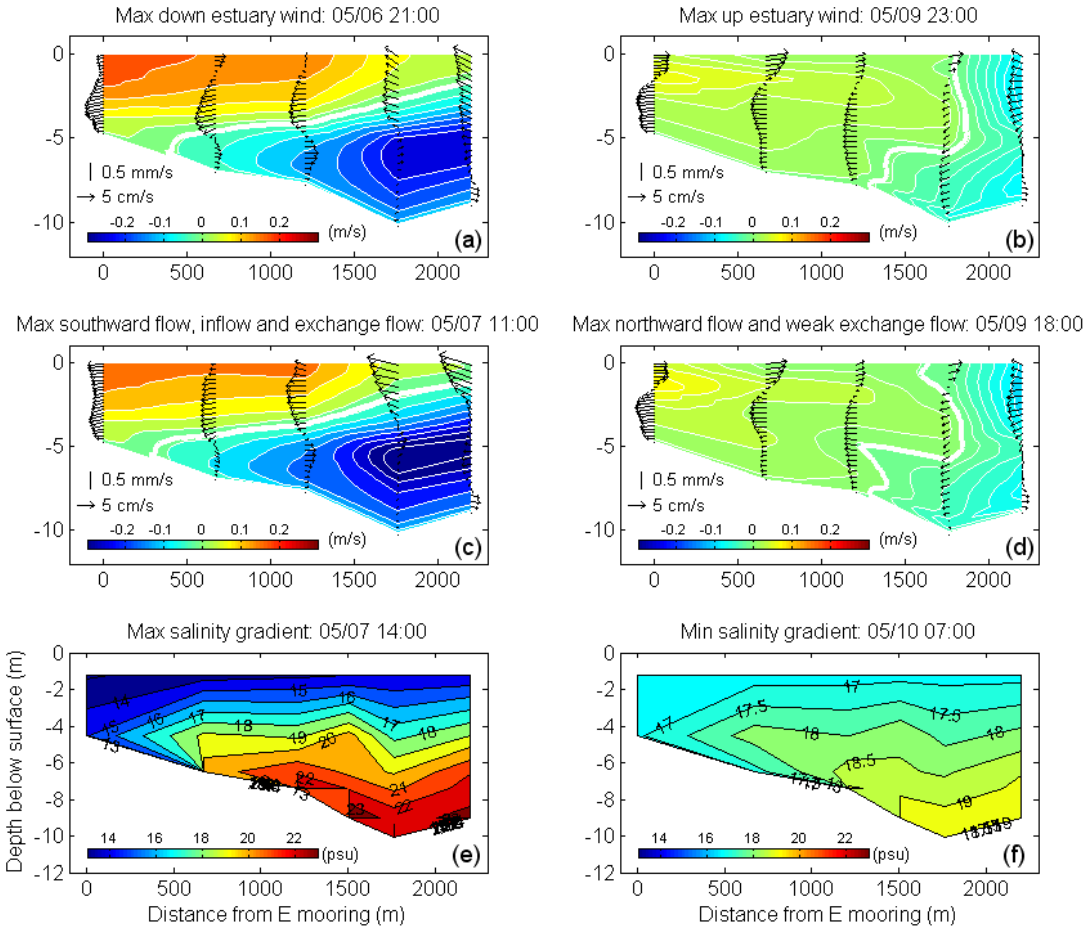

Figure 9: Velocity and salinity snap shots on subtidal scale over transect 1 (looking into the estuary). (a-d): Snap shots of velocity at times indicated in its individual titles. The color filled contours describe along channel velocities and the vectors scale with cross channel velocities. The thick white lines mark zero along channel velocity. The along channel, cross channel and vertical velocities are in different units as shown in the figure. (e-f): Snap shots of interpolated salinity at times indicated in its individual titles. Contours are in the unit of psu and color bars have the same range from 13 psu to 23 psu. Note that panel (e) is contoured every 1 psu while panel (f) is contoured every 0.5 psu.

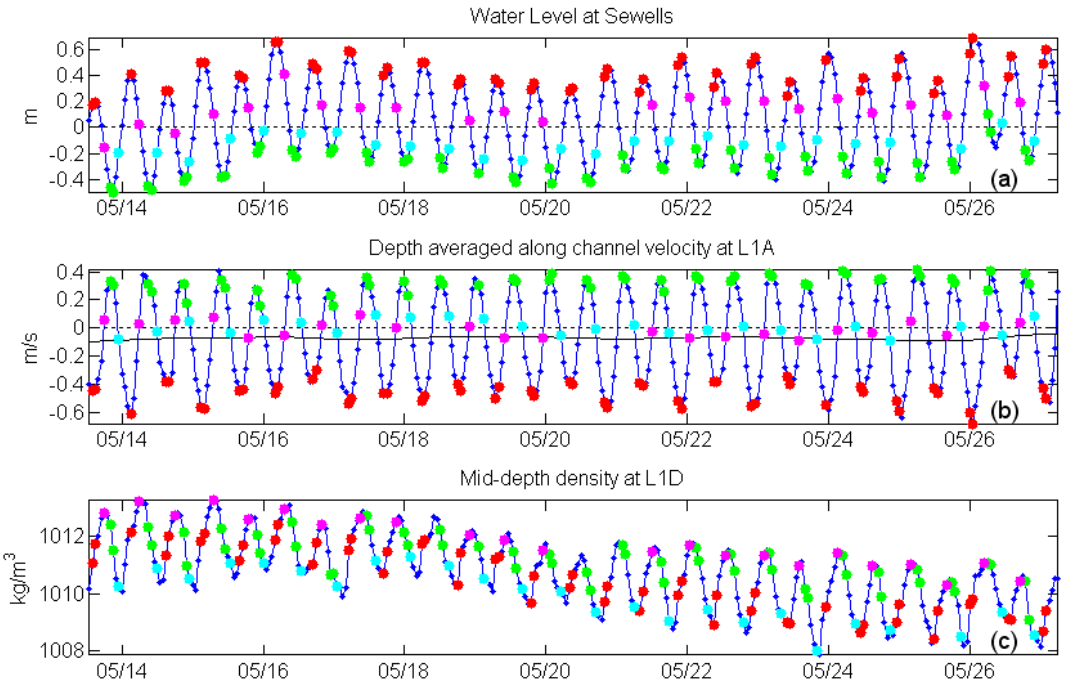

Figure 10: Time series of sea level, velocity and density during the low wind, spring period. Red dots mark max flood; green dots mark max ebb. Magenta dots represent slack after flood and cyan dots represent slack after ebb. (a): Time series of water level at Sewells Point (location shown in Figure 1 (b)). (b): Time series of depth averaged along channel velocity at L1A. Black solid line is low pass filtered velocity. (c): Time series of density at mid-depth of L1D.

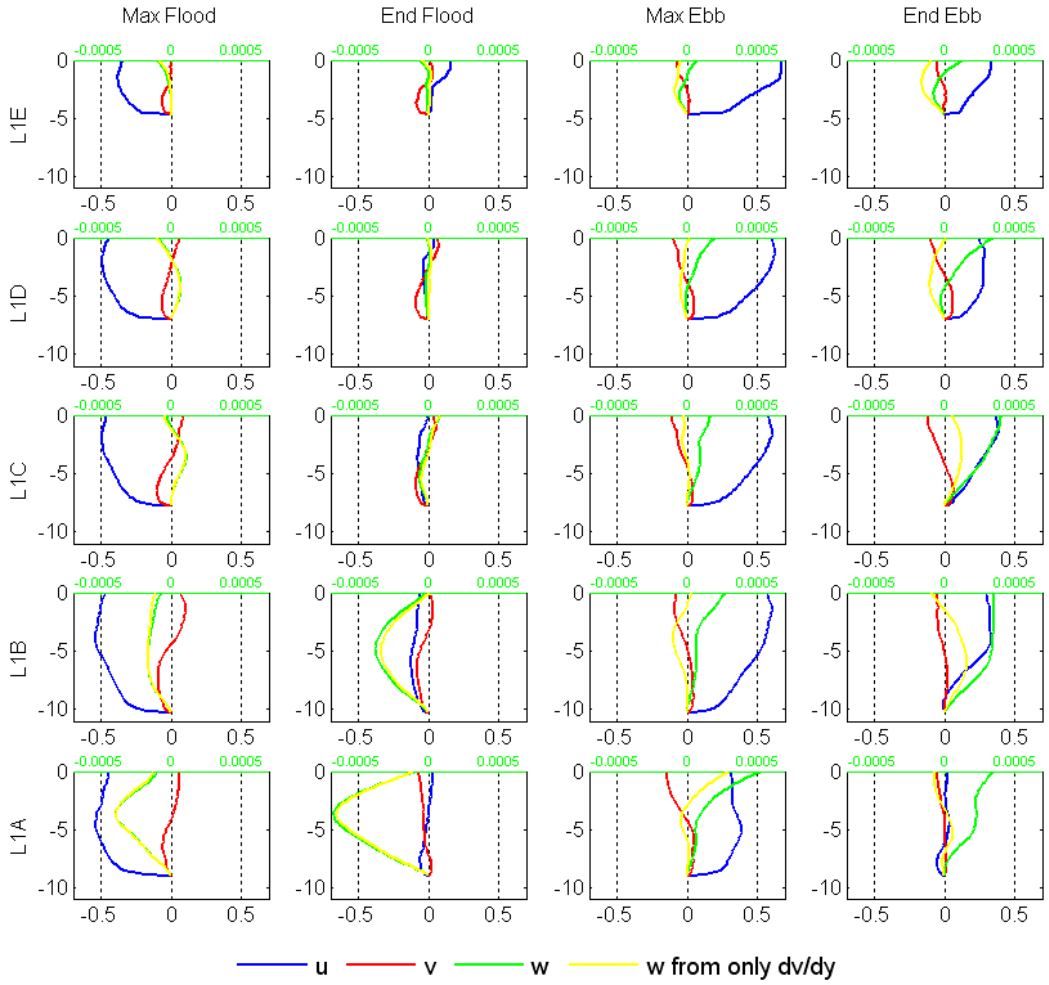

Figure 11: Velocity profiles averaged over the low wind, spring tide period following the tidal phases in Figure 10. The location of the moorings is indicated by their IDs on the left and the phases in the tidal cycle are shown on the top. Blue line is the along channel velocity and red line is the cross channel velocity. Their values are both shown on the bottom of each individual panel with bounds [-0.7 0.7] m/s. The green line is vertical velocity calculated from both du/dx and dv/dy and the yellow line is vertical velocity calculated using only dv/dy. Their values are indicated on the top of each panel with the green ticks. The unit is also m/s. The y-axis is depth below water surface and has the unit of m.

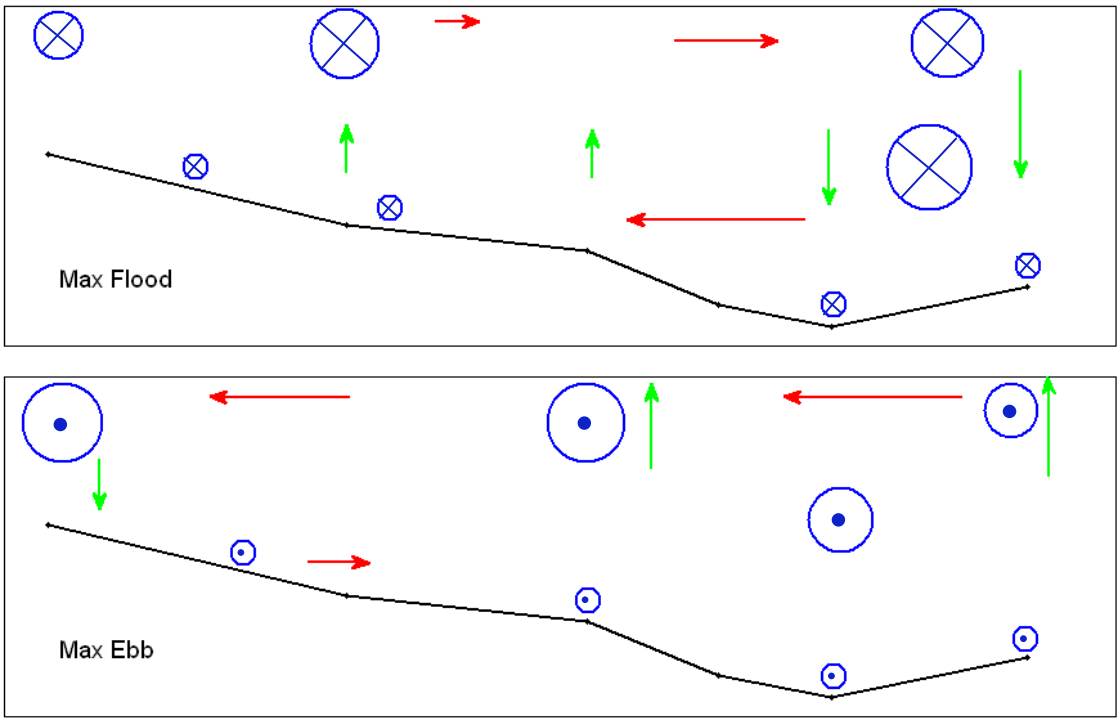

Figure 12: A schematic view of the velocity field at max flood and ebb. Blue circles represent along channel velocity, red arrows represent cross channel velocity and green arrows represent vertical velocity. The sizes of the shapes are drawn to show the relative speed in each direction, but no comparison of magnitude should be made among different directions.

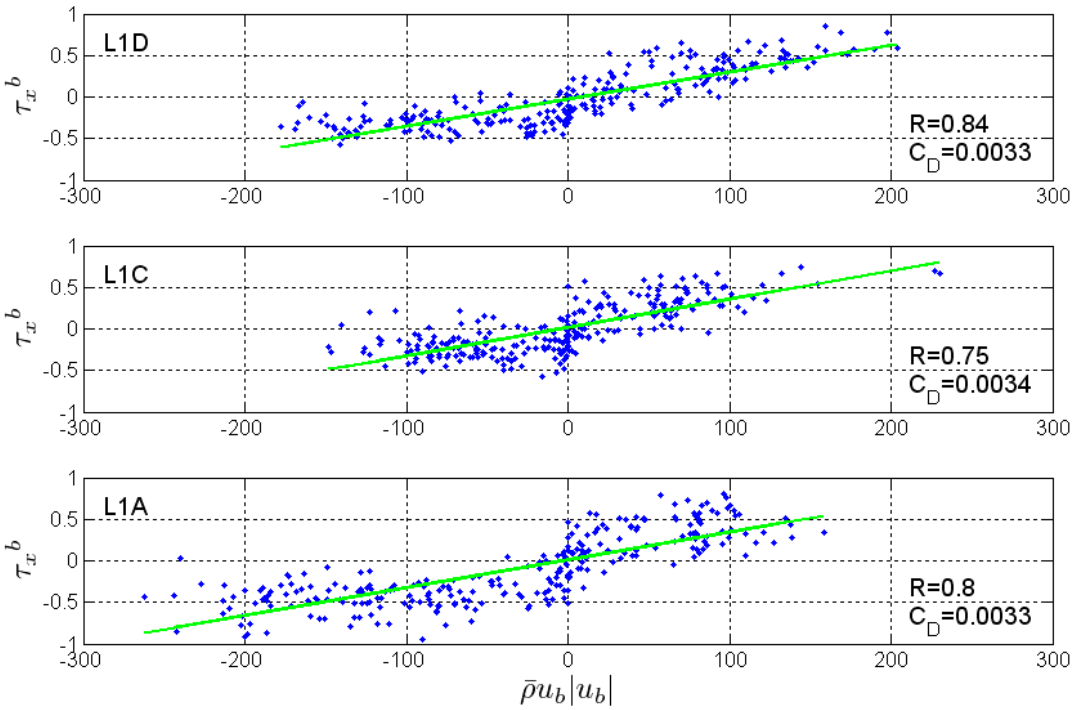

Figure 13: The relation between along channel bottom stress integrated from the momentum equation (τ_x^b) and bottom stress calculated from quadratic drag law ($\bar{\rho}u_b|u_b|$) indicates the estimated bottom drag C_D. The unit for both axes is $\left({}^{kg}/_{m^3}\right) \times \left({}^{m^2}/_{s^2}\right)$. The green line is the best linear fit and its slope is the estimated C_D for the location shown. The correlation coefficient is also shown.

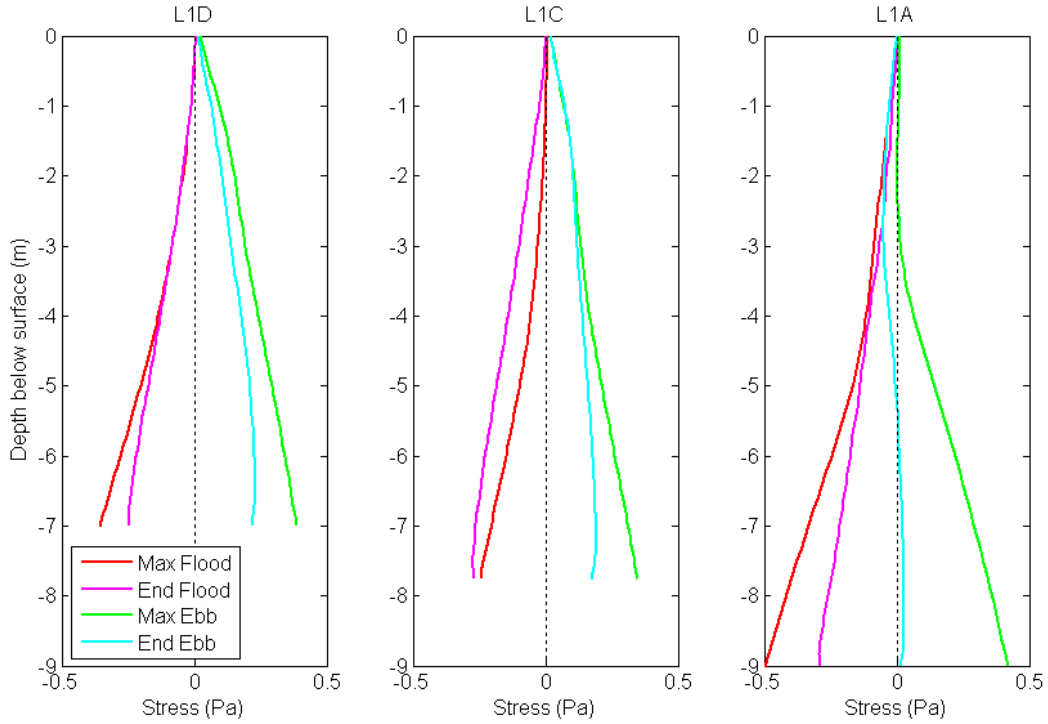

Figure 14: Stress profiles averaged at four tidal phases over the low wind, spring tide piece.

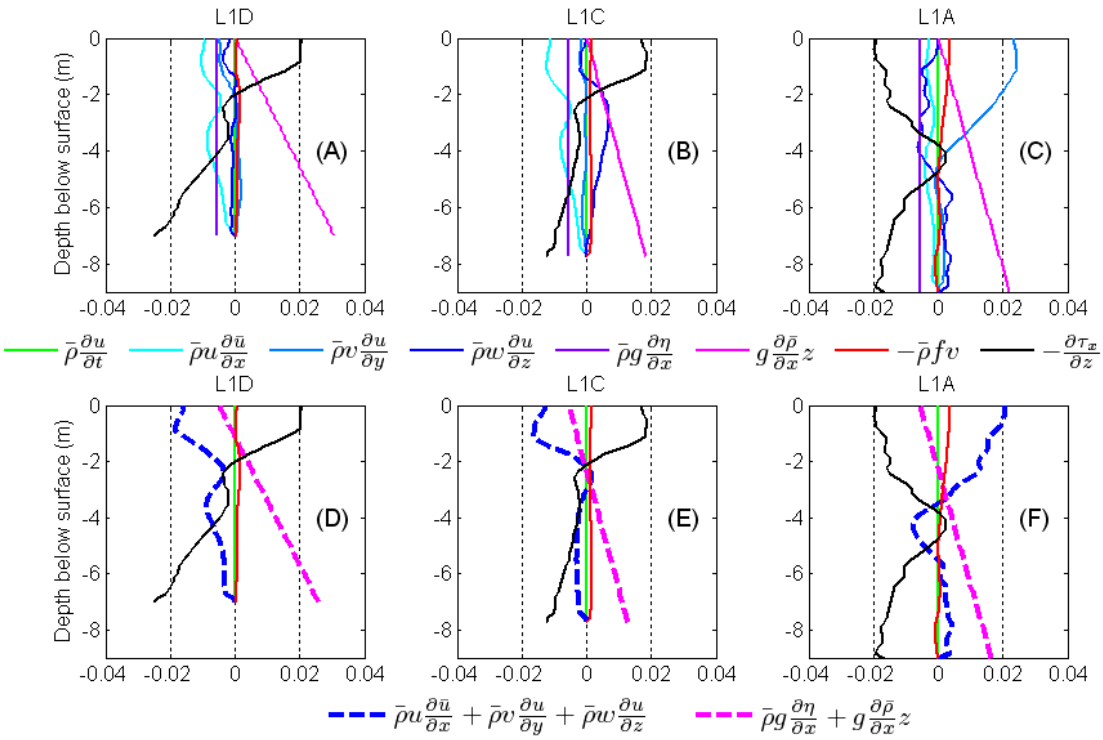

Figure 15: Subtidal forces in the along channel momentum equation (Eq.3) averaged during the low wind, spring tide piece for the 3 locations. Solid lines represent different individual terms in the momentum equation; Thick slash lines describe the sum of similar terms. Unit for x-axis is $\left({}^{kg}/_{m^3}\right) \times \left({}^{m}/_{s^2}\right)$ and unit for y-axis is m (depth below water surface).

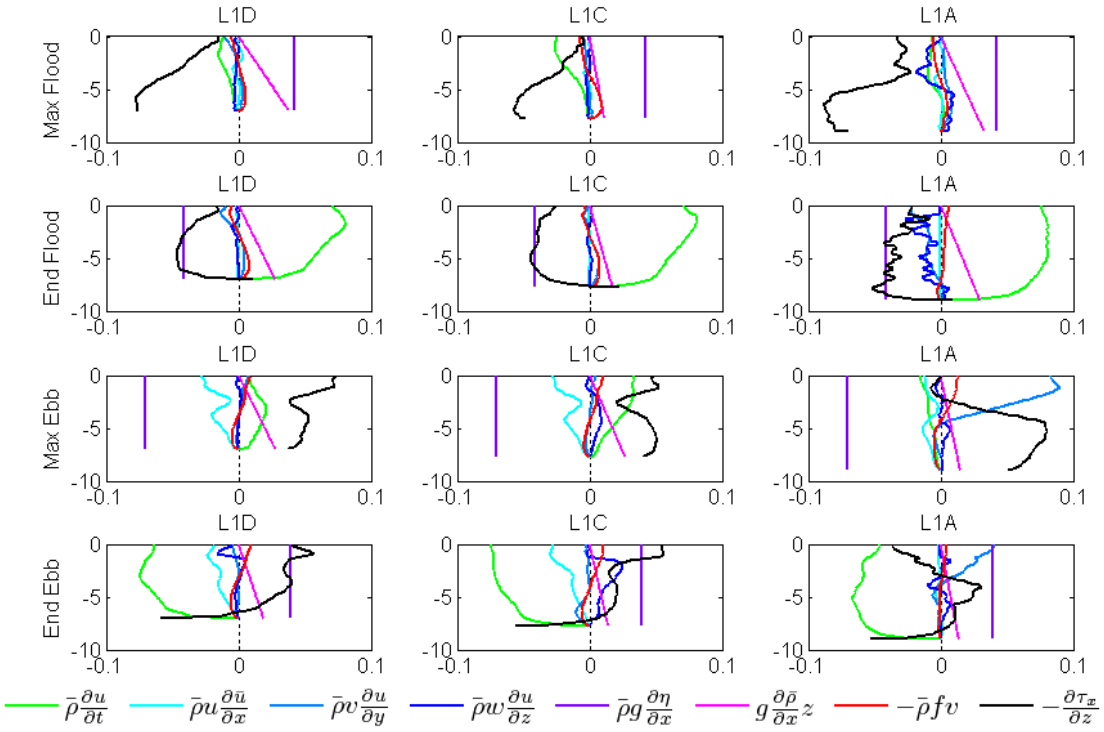

Figure 16: Forces in the along channel momentum equation averaged over the four tidal phases at the three moorings. Colors represent difference terms in Eq.3. Unit for x-axis is $\left({}^{kg}/_{m^3}\right) \times \left({}^{m}/_{s^2}\right)$ and unit for y-axis is m (depth below water surface).

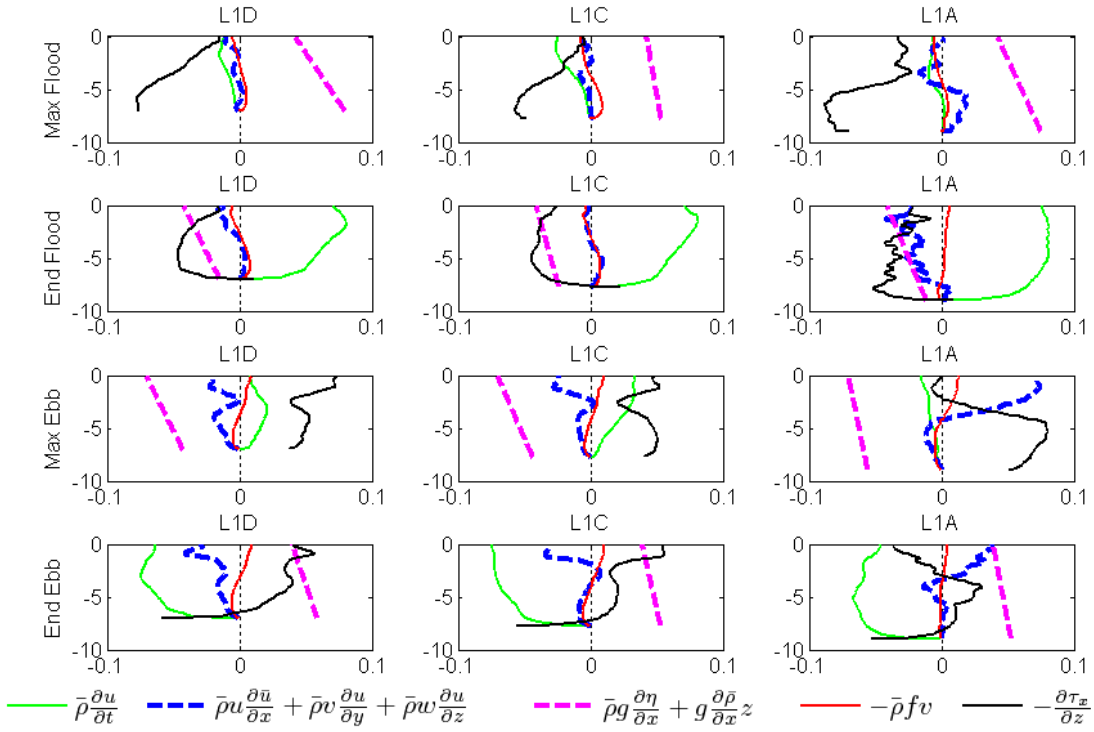

Figure 17: Forces in the along channel momentum equation averaged over the four tidal phases at the three moorings. Solid lines represent different individual terms in the momentum equation; thick slash lines describe the sum of similar terms. Unit for x-axis is $\left({}^{kg}/_{m^3}\right) \times \left({}^{m}/_{s^2}\right)$ and unit for y-axis is m (depth below water surface).

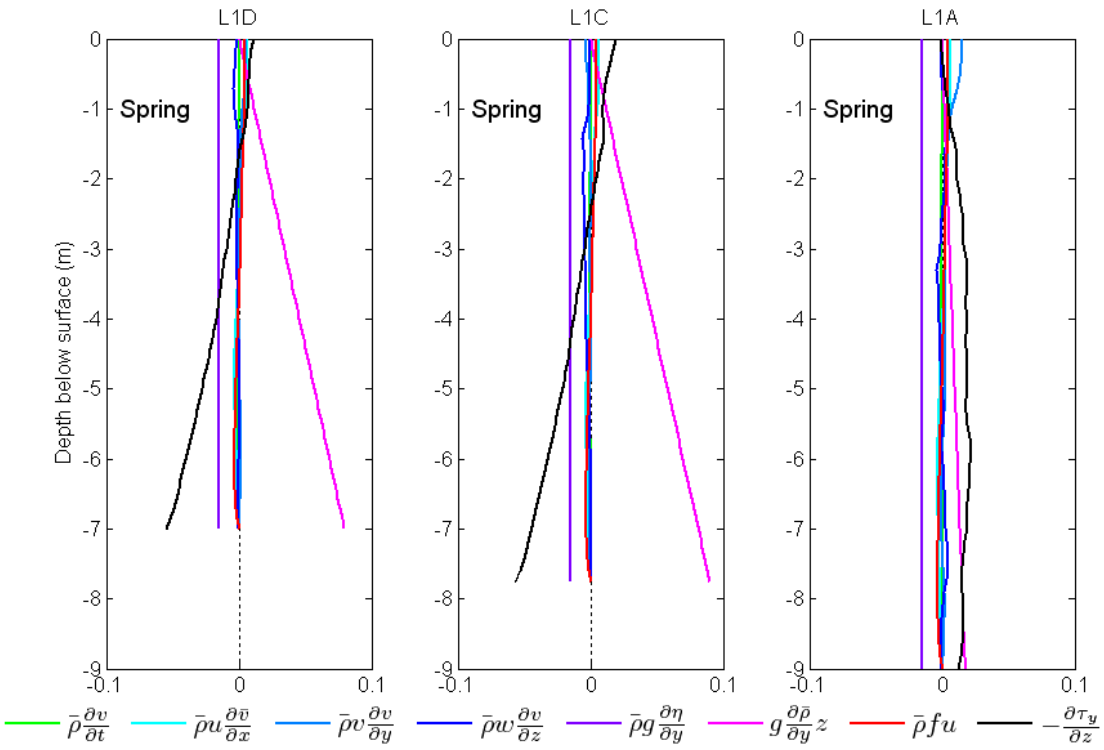

Figure 18: Subtidal forces in the cross channel momentum equation (Eq.3) averaged during the low wind, spring tide piece for the 3 locations. Colors represent different individual terms in the momentum equation Unit for x-axis is $\left({}^{kg}/_{m^3}\right) \times \left({}^{m}/_{s^2}\right)$ and unit for y-axis is m (depth below water surface).

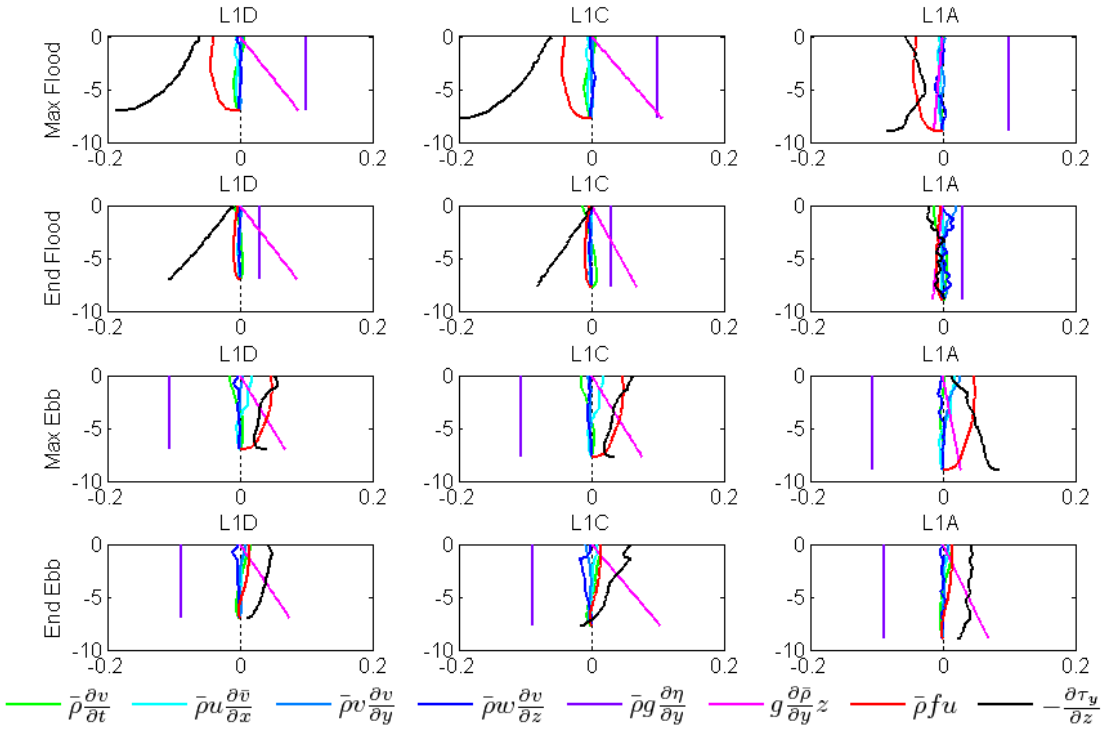

Figure 19: Forces in the cross channel momentum equation averaged over the four tidal phases at the three moorings. Colors represent difference terms in Eq.3. Unit for x-axis is $\left({}^{kg}/_{m^3}\right) \times \left({}^{m}/_{s^2}\right)$ and unit for y-axis is m (depth below water surface).

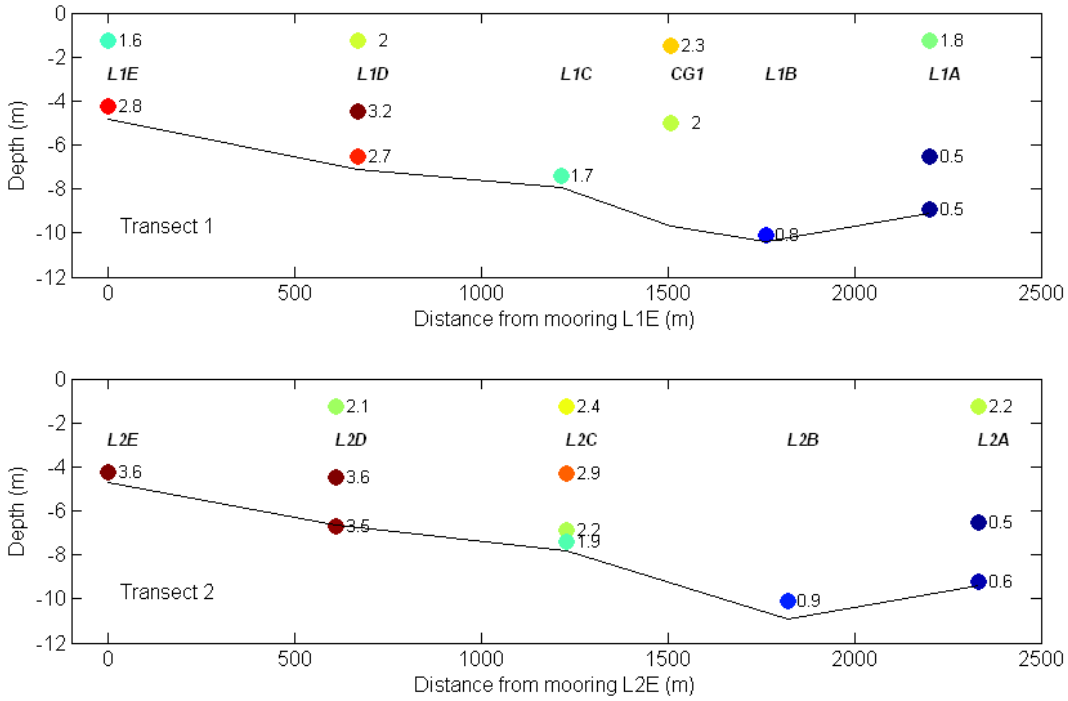

Figure 20: Scopes of salinity fluctuation averaged within tidal cycles over the whole record. The unit is psu. The numbers and colors indicate the magnitude of the difference between maximum salinity and minimum salinity during the tidal cycle.

References

Chant, Robert J, Wayne R Geyer, Robert Houghton, Elias Hunter, and James Lerczak. "Estuarine Boundary Layer Mixing Processes: Insights from Dye Experiments." Jounal of Physical Oceanography, 2007: 1859-1877.

Geyer, W. R, R. Chant, and R. Houghton. "Tidal and spring-neap variations in horizontal dispersion in a partically mixed estuary." Journal of Geophysical Research, 2008.

Geyer, W. Rockwell, John H Trowbridge, and Melissa M Bowen. "The Dynamics of a Partially Mixed Estuary." Journal of Physical Oceanography, 2000: 2035-2048.

Hansen, Donald V, and Maurice Rattray. "Gravitational Circulation in Straits and Estuaries." Journal of Marine Research, 1965: 104-122.

Large, W. G, and S Pond. "Open Ocean Momentum Flux Measurements in Moderate to Strong Winds." Journal of Physical Oceanography, 1981: 324-336.

Lerczak, James A, and W. Rockwell Geyer. "Modeling the Lateral Circulation in Straight, Stratified Estuaries." Journal of Physical Oceanography, 2004: 1410-1428.

Mac Cready, Parker, and Geyer W. Rockwell. "Advances in Estuarine Physics." The Annual Review of Marine Science, 2010: 35-58.

NOAA. NOAA Ocean Service Education. March 25, 2008. http://oceanservice.noaa.gov/education/kits/estuaries/media/supp_estuar04_coastal.html (accessed August 15, 2011).

Pritchard, D. W. "The Dynamic Structure of a Coastal Plain Estuary." Journal of Marine Research, 1956: 33-42.

Scully, Malcolm E, W. Rockwell Geyer, and James A Lerczak. "The Influence of Lateral Advection on the Residual Esturine Circulation: A Numerical Modeling Study of the Hudson River Estuary." Journal of Physical Oceanography, 2009: 107-124.

Trowbridge, J. H, Geyer W. R, M. M Bowen, and Williams A. J. "Near-Bottom Turbulence Measurements in a Partially Mixed Estuary: Turbulent Energy Balance, Velocity Structure, and Along-Channel Momentum Balance." Journal of Physical Oceanography, 1999: 3056-3072.

Valle-Levinson, Arnoldo, Kuo-Chuin Wong, and Kamazima M.M. Lwiza. "Fortnightly Variability in the Transverse Dynamics of a Coastal Plain Estuary." Journal of Geophysical Research, 2000: 3413-3424.